Report No.
UCB/SEMM-2012/01

Structural Engineering
Mechanics and Materials

Three-Dimensional Nonlinear Cyclic Beam-Truss Model for Non-Planar Reinforced Concrete Walls

By

Yuan Lu and Marios Panagiotou

April 2012

Department of Civil and Environmental Engineering
University of California, Berkeley

Abstract

A three-dimensional (3D) nonlinear cyclic model for non-planar reinforced concrete walls is presented. The model uses 3D nonlinear Euler-Bernoulli fiber-section beam-column elements representing steel and concrete in the vertical and horizontal directions, and nonlinear trusses to represent the diagonal field of concrete in compression. The model represents the effects of flexure-shear interaction by computing the stress and strains in the horizontal directions, and accounts for bi-axial effects on the behavior of concrete diagonals in compression and mesh size effects. It is validated by comparing the experimentally measured and numerically computed response of three reinforced concrete wall specimens having a T-, C-, and I-shape section, respectively, with the response of the latter two characterized by crushing of the concrete in the diagonal direction. The computed response using the model developed here is compared with the computed response using Euler-Bernoulli fiber-section beam-column models. The overall force-deformation and local strain responses are presented.

Introduction

Reinforced concrete (RC) walls are one of the most common elements used in structures to resist loads and develop expected deformations during earthquake excitation. The computation of their nonlinear cyclic response is of significant interest to both practicing engineers and researchers. This task is particularly challenging for non-planar RC walls, commonly used in medium- and high-rise construction, because their response is affected more than planar walls by three-dimensional (3D) stress and strain state when subjected to uni-axial or multi-axial loading representative of earthquake excitation. The computation of the response of non-planar RC walls can be even more challenging when it is affected significantly by flexure shear interaction (FSI). Here, FSI is described as the combination of axial, flexural, and shear load on these structural elements, which results in a multi-axial stress and strain state and coupling of nonlinearities in the behavior of concrete in compression. The FSI may significantly affect the cyclic behavior of RC non-planar walls in terms of strength, stiffness, deformation capacity, softening response, and strains developed in steel and concrete.

Modeling approaches for non-planar RC walls may be divided in five main categories: (i) lumped plasticity models; (ii) fiber-section beam-column (frame) element models; (iii) wide column models known also as equivalent frame models; (iv) truss or lattice models; (v) models with beams and trusses; and (vi) finite element (FE) models using either plane stress or solid elements.

Lumped plasticity models (Giberson 1969) use beam elements that develop all the plasticity in nonlinear springs located at their ends and have been used to model non-planar walls in a two-dimensional (2D) analysis (Hidalgo et al. 2002). In these models, flexure-shear interaction can be considered using empirically calibrated nonlinear springs. These models do not account for multi-axial force interaction.

Stiffness-based nonlinear fiber-section beam element models (also called displacement-based nonlinear fiber-section beam element models), were first proposed in the 1970s (Taylor 1977, Kang 1977) and flexibility-based (also called force-based elements) were later developed (Zeris and Mahin 1988, Spacone et al. 1992). Force-based beam elements considering nonlinear geometry have also been developed (Neuenhofer and Filippou 1998). Two- (Petrangeli 1999a, 1999b) and three-dimensional (Martinelli 2008) fiber-section beam elements that model the inelastic behavior of the transverse steel reinforcement and represent FSI using equilibrium, specific assumptions for the shear strain field, and biaxial concrete material laws have also been developed. Such models have been used to model non-planar walls experimentally tested under uni-axial cyclic loading. Nonlinear fiber-section beam models that use the plane-section-remain-plane assumption and a linear empirical relationship between shear force and shear deformations that is decoupled from axial and flexural deformations have been used in 2D analysis of T-shape walls subjected to uni-axial cyclic loading (Orackal and Wallace 2006). Fiber-section

beam elements considering linear elastic behavior in shear and torsion have been used to model the multi-axial cyclic behavior of non-planar walls (Mazars et al. 2006).

Linear elastic frame models have been developed for the analysis of planar and non-planar walls with openings or coupled with beams (Clough et al. 1964, MacLeod 1973). Beyer et al. (2008b) presented a nonlinear frame model used to reproduce the experimental response of RC wall with a U-shape section. This U-wall is also considered here. This model used nonlinear Euler-Bernoulli fiber-section vertical beam elements and rigid horizontal beam elements connected with linear shear and torsional springs.

Nonlinear truss models have been used for 2D analysis of planar walls (To et al. 2003, Park and Eom 2007, Panagiotou et al. 2012). Three-dimensional truss models (also called lattice models) have been used to model RC columns, beams, and frames (Miki and Niwa 2004).

Barbosa (2011) recently presented a 3D model for planar RC walls consisting of nonlinear fiber-section Euler-Bernoulli beams and nonlinear truss elements. In this model, the nonlinear beam elements represented the boundary elements while nonlinear vertical truss elements were used to model the concrete and steel of the inner regions of the walls. In parallel to the vertical truss elements, linear elastic beam elements were used to model the out-of-plane flexural rigidity of the walls. In addition, truss elements were used to model the horizontal reinforcement and the diagonal stress field of concrete without accounting for the instantaneous biaxial effects on the behavior of concrete in compression.

Nonlinear 2D monotonic (Cervenka and Gerstle 1971 and 1972) and cyclic (Vallenas et al. 1979) FE models of RC structures using plane-stress elements were first introduced four decades ago and were validated using experimental results. Nonlinear 2D FE models for RC that use monotonic or cyclic smeared crack, or/and discrete crack approaches, plasticity models, or non-local models have been developed (Bazant and Planas 1998, Maekawa et al. 2003, Koutromanos and Shing 2012). The complexity and computational effort required in nonlinear 3D FE modeling increases significantly compared to 2D models. These methods also have their limitations and are used mainly by academics and specialized consultants. Three-dimensional FE studies appeared for first time in the 1970s (Suidan and Schnobrich 1973) and thereafter have considered the monotonic behavior of flexural dominated or shear-critical beams (Milford and Schnobrich 1985, Vidosa et al. 1991, Pagnoni et al. 1992, Barzegar and Maddipudi 1997). Nonlinear 3D cyclic FE models of shear-critical columns (Ozbolt et al. 2001) and beam-column sub-assemblages (Maekawa et al. 2003, Lykidis and Spiliopoulos 2008, Eligehausen et al. 2009) have also been developed. The authors are not aware of any 3D discrete crack cyclic model of an experimentally tested shear-critical RC component (e.g., beam, column, wall, joint, etc.).

There have been numerous 2D nonlinear FE studies of planar walls subjected to cyclic loading (Sittipunt and Wood 1995, Kwak and Kim 2004, Vecchio 2002, 2007). Vidosa et al. (1991) compared the experimentally measured and computed monotonic response, using a 3D nonlinear FE model, for a

flexural dominated planar RC wall. Palermo and Vecchio (2002, 2007) compared the experimentally measured and numerically computed cyclic response using a 2D nonlinear FE model of a squat non-planar wall with wide flanges subjected to cyclic loading. El-Tawil et al. (2002) and Hassan and El-Tawil (2003) conducted 3D FE studies of planar walls as well as of a T-shape section wall subjected to uni-axial loading, also considered here, using plane-stress elements and reported very good agreement between computed and measured response in terms of strains along the flange of the wall; however, the force-deformation response was not presented in their study. Mosalam et al. (2003) conducted 3D nonlinear FE monotonic analysis to verify the splitting failure caused planar lightweight concrete planar shear walls with embedded steel members. Balkaya and Kalkan (2004) conducted a 3D monotonic analysis of a RC wall building using nonlinear shell elements for the walls and the slabs; this study did not include any comparison with experimental results. Ile and Reynouard (2005) conducted a 3D FE analysis, using thin shell elements, of a C-shape wall subjected to bi-directional cyclic load reversals.

This report describes a nonlinear beam-truss modeling approach for non-planar RC walls subjected to cyclic uni-axial or multi-axial loading. The main objective of the proposed model is as follows: (i) to compute the post cracking three-dimensional behavior of non-planar RC walls; and (ii) to model FSI accounting for mesh size effects. The model approximates FSI by modeling the effect of normal tensile strain on the stress-strain relationship of concrete in compression as reported by Vecchio and Collins (1986), but it incorporates the normal strain reduction factor as a function of the gage length as proposed by Panagiotou et al. (2012). Compared to the beam-truss model reported by Barbosa (2011) and the nonlinear frame model of Beyer et al. (2008b), the model developed here accounts for the instantaneous bi-axial strain field in the behavior of diagonal concrete in compression. Moreover this model uses nonlinear beam elements for all vertical and horizontal elements, and accounts for mesh size effects. To test the efficacy of the model, the experimentally measured and computed response of three case studies are considered: (i) a wall with a T-shape section subjected to uni-axial cyclic loading with significant contribution of the flange to the response; (ii) a U-shape section wall subjected to multi-axial cyclic loading, which failed by crushing of concrete in the diagonal direction; and (iii) an I-shape section wall subjected to uni-axial loading, which failed with diagonal crushing of the web. The global responses in terms of lateral force-lateral displacement as well as the more localized strain responses are presented.

Nonlinear Beam-Truss Modeling Approach

The model approach developed herein uses nonlinear fiber-section Euler Bernoulli beam elements in the vertical and horizontal directions, termed beams from this point, and truss elements in the diagonals of the panels formed by the horizontal and vertical beam elements. Consider the T-section wall shown in Figure 1(a) where its length along the *x*- and *y*-axis is L_x and L_y, respectively. The thickness of the rectangular section segments of the wall parallel to the *x*- and *y*-axes is t_x and t_y, respectively. The height of the wall is *H*. Figure 1(b) shows the beam-truss model of this wall. Nine lines of vertical beam elements were used, with five in each of the two segments of the T-wall. Line BF is common for the two segments. Each of the vertical and horizontal beam elements model the concrete and steel included in the section areas they represent. The nine sections of the corresponding vertical line of elements and the fifteen sections of the corresponding horizontal lines of elements are shown in Figure 1(a). Panel A parallel to *x*-axis is shown with bold lines in Figure 1(a), and the reinforcing details of this panel are shown in Figure 1(c). Figures 1(d) and (e) show the section areas of each of the vertical and horizontal beams. A minimum number of four vertical lines of elements were used along each segment of the non-planar walls described below. The effect mesh refinement is presented in the section *Effect of Mesh Refinement*. In this study, each fiber section used 24 fibers in a 6 × 4 grid to represent the concrete, and a single fiber to represent each reinforcing steel bar. For each vertical and horizontal beam element, a linear elastic torsional rigidity equal to 0.01 J_g was used, where J_g is the gross section torsional rigidity. The small value of torsional rigidity is used for better numerical stability of the model.

In addition to the vertical and horizontal beam elements, concrete truss elements were used for all diagonals to model the compressive field of concrete in the corresponding direction. The angle of the diagonals in respect to the horizontals is θ_d, see Figure 1(g). In this study, θ_d ranged between 40° and 50°. The effect of θ_d is discussed in section *Effect of the Angle of the Diagonal Truss Elements*. The tensile field of concrete in the diagonals is not modeled and the sensitivity to this is discussed in section *Effect of Tension Strength of the Diagonal Truss Elements*. The area of each diagonal is the product of the effective width b_{eff}, see Figure 1(f) and (g), and the thickness of the panel t_x. The effective width of the diagonal b_{eff} depends on the dimensions of the panel and thus on the angle of the diagonal, θ_d.

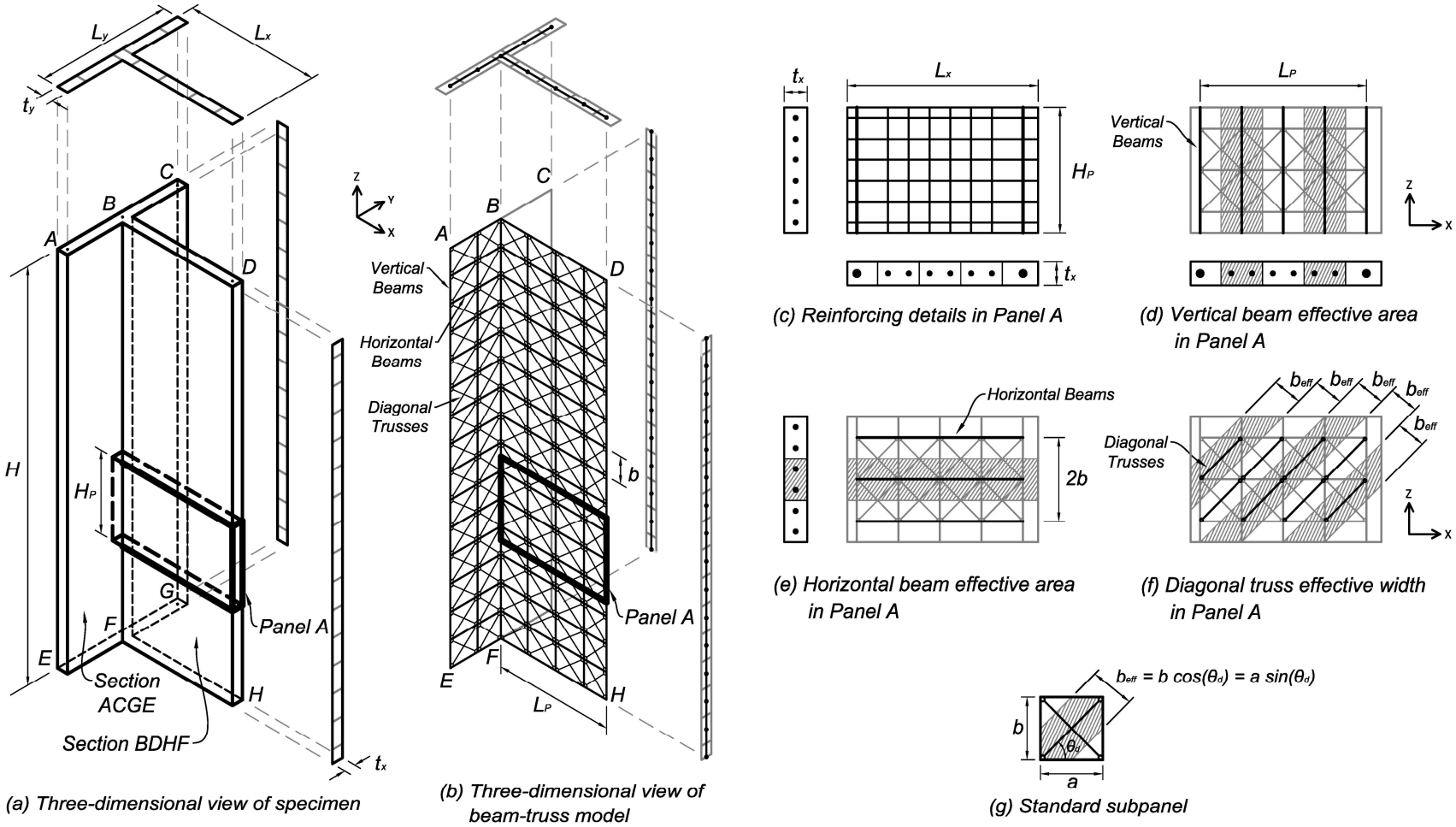

Figure 1. Three-dimensional view of the beam-truss model approach for a T-shape section wall.

Material Constitutive Stress-Strain Relationships

Concrete Model for Vertical and Horizontal Beams Elements

The stress-strain relation of concrete used in the vertical and horizontal beam elements is shown in Figure 2, where $f_c^{'}$ is the compressive strength of unconfined concrete occurring at strain $\varepsilon_0 = 0.2\%$. The compressive stress-strain relation up to $f_c^{'}$ is based on the Fujii concrete model (Hoshikuma et al. 1997); see Equation 1 in Figure 2. The initial concrete modulus is $E_c = 5000\sqrt{f_c^{'}}\,(MPa)$. For unconfined concrete, after reaching $f_c^{'}$, the compressive stress decreases linearly to zero at strain ε_u. The value of ε_u accounts for mesh size effects, as explained in section *Mesh Size Effects*, with $\varepsilon_u = 0.4\%$ for a reference element length L_R = 600 mm. For confined concrete, the peak compressive stress f_{cc} occurring at strain ε_{co}, and the strain ε_{cs} at which softening initiates is calculated based on Mander et al. (1983). The stress-strain relation of confined concrete during loading up to $f_c^{'}$ is the same as the unconfined concrete. During loading from $f_c^{'}$ to f_{cc}, the stress-strain relation is described by Equation 1. The confined concrete stress remains constant and equal to f_{cc} for strains between ε_{co} and ε_{cs}. For strains larger than ε_{cs}, the stress softens linearly to zero at a strain ε_{cu}. The value of ε_{cu} accounts for mesh size effects, with $\varepsilon_{cu} = \varepsilon_{cs} + 0.2\%$ for L_R = 600 mm.

The tension stress-strain relationship during loading is linear until it reaches the tensile strength of concrete $f_t = 0.33\sqrt{f_c^{'}}$ in MPa. After this point, the concrete softens based on Equation 2, shown in Figure 2 (Stevens et al. 1991). The parameter $M = C_t \dfrac{\rho_s}{d_b}$ controls the rate of softening, with C_t = 75mm, ρ_s the steel ratio in the direction parallel to the beam element, and d_b the diameter of the rebar of interest. The exponential decay factor λ_t is described in Equation 2.

Upon unloading from a compressive strain, the tangent modulus is $E_u = 0.5 \cdot E_c + 0.5 \cdot (f / \varepsilon)$ until reaching zero stress, which then reloads linearly to the point with the largest tensile strain that occurred before. The unloading from a tensile strain is linear with a tangent modulus E_c until reaching zero stress. After this, the material loads in compression and targets a stress equal to $\alpha \cdot f_t$ at zero strain with $a = 0.5$. Thereafter, the material loads linearly to the point where the peak compressive strain occurred. In the case where the stress of this target point is less than $\alpha \cdot f_t$, the material reloads directly

to the point where peak compressive strain occurred without passing through the point with stress $\alpha \cdot f_t$ at zero strain.

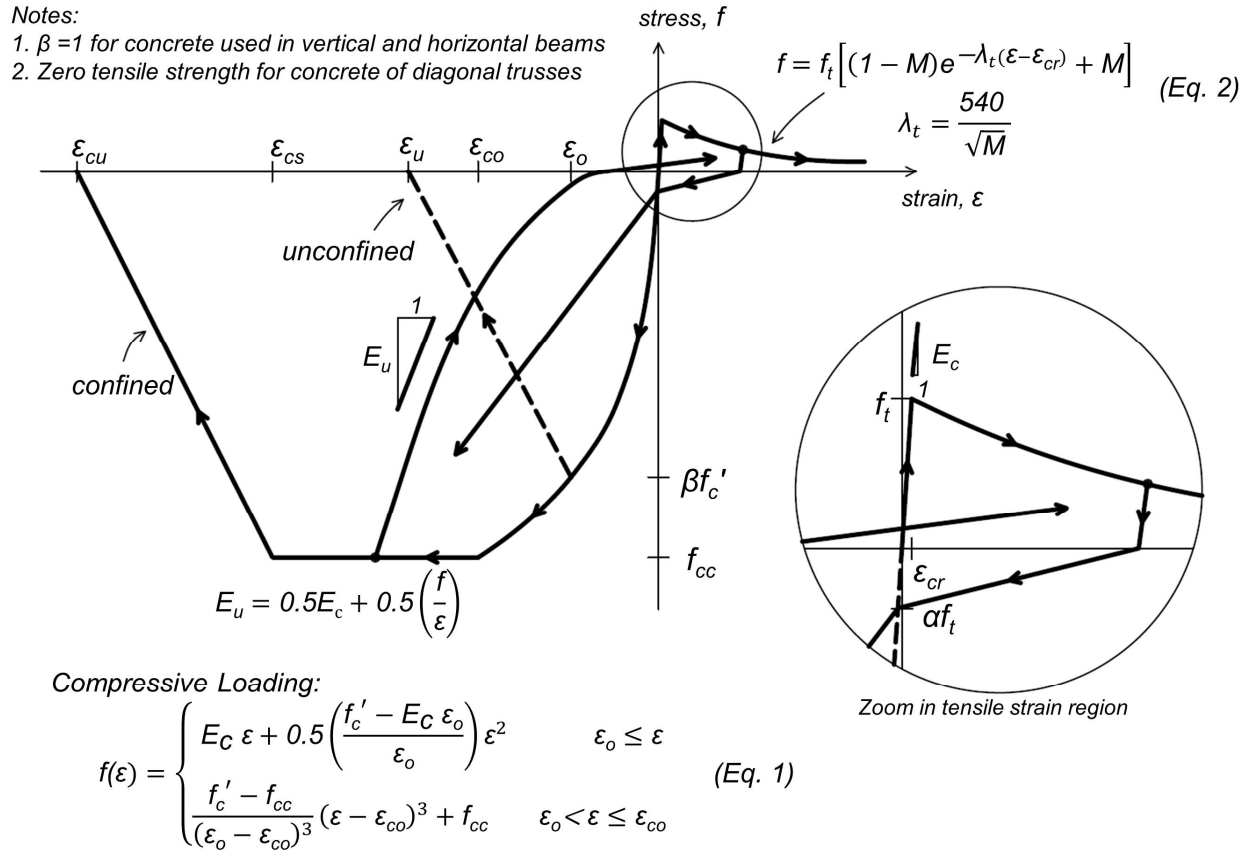

$$f = f_t\left[(1-M)e^{-\lambda_t(\varepsilon-\varepsilon_{cr})} + M\right] \qquad \lambda_t = \frac{540}{\sqrt{M}}$$

$$E_u = 0.5E_c + 0.5\left(\frac{f}{\varepsilon}\right)$$

$$f(\varepsilon) = \begin{cases} E_C\,\varepsilon + 0.5\left(\dfrac{f_c' - E_C\,\varepsilon_o}{\varepsilon_o}\right)\varepsilon^2 & \varepsilon_o \le \varepsilon \\ \dfrac{f_c' - f_{cc}}{(\varepsilon_o - \varepsilon_{co})^3}(\varepsilon - \varepsilon_{co})^3 + f_{cc} & \varepsilon_o < \varepsilon \le \varepsilon_{co} \end{cases}$$

Figure 2. Stress-strain relationship of concrete material models.

Concrete Model for Diagonal Truss Elements

The concrete material model used for the truss elements has two differences compared to that used for the beam elements: (i) it has zero tensile strength; and (ii) it accounts for the bi-axial strain field on the concrete compressive behavior as described by Vecchio and Collins (1986). Thus, the compressive stress-strain behavior is dependent on the strain, ε_n, normal to the axes of the truss element. For truss element e_1 extending from node 1 to node 2 shown in Figure 3(a), ε_n is computed using the zero-stiffness gauge element extending from the mid-length of the element to nodes 3 and 4, g_1 and g_2, respectively. The instantaneous compressive stress of element e_1 is multiplied by the factor β determined from the instantaneous normal strain ε_n, which is the average of the strain measured with the gauge elements g_1 and g_2. The angle θ_g is the angle formed between the truss and the gauge elements; values of θ_g close to 90° are suggested. When $\varepsilon_n > 0$, the relationship between β and ε_n is tri-linear as shown in Figure 3(b).

For this study, the relation between β and ε_n depends on the length of the gauge elements, as proposed by Panagiotou et al. (2012), and are discussed in section *Mesh Size Effects*. For a reference length of L_R = 600 mm, β_{int} = 0.3, ε_{int} = 1%, β_{res} = 0.1, and ε_{res} = 2.5%.

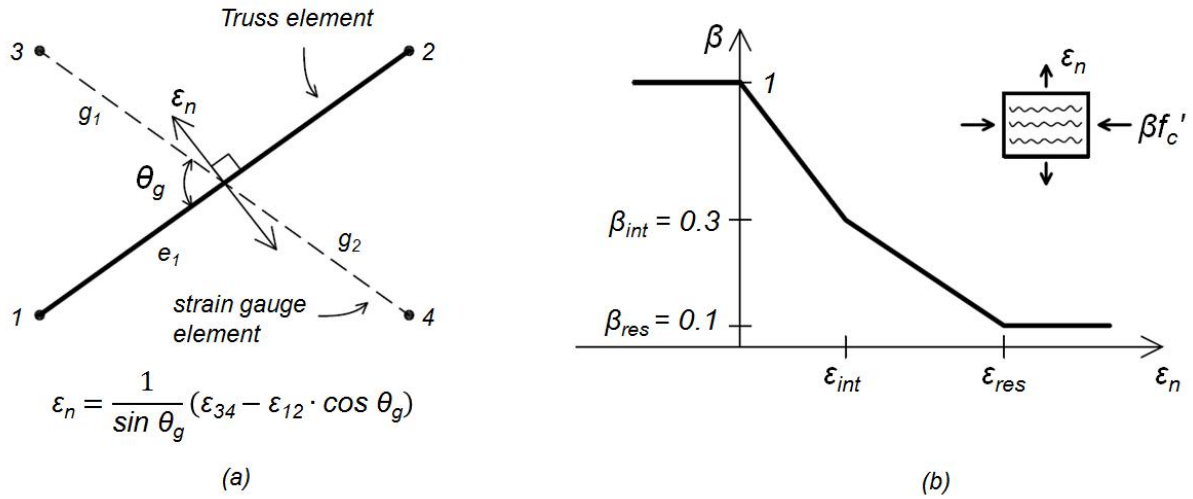

Figure 3. (a) Truss model accounting for biaxial effects in the compressive stress-strain behavior of concrete; and (b) Relation between concrete compressive stress reduction factor, β, and normal strain, ε_n.

Mesh Size Effects

The computation of the nonlinear response of structural elements modeled using material models that include strength-degrading behavior strongly depends on the size of the elements used in the analysis. This problem is addressed by making the strength-degrading branch of the stress-strain relationships of the materials a function of the size of the elements or by nonlocal continuum modeling (Bazant and Ceolin 1979; Pietruszczak and Mroz 1981; Bazant and Planas 1998). Here, the concept of concrete fracture energy is used to determine the slope of the softening branch of the concrete compressive stress-strain behavior. Figure 4(a) shows a concrete element subjected to uniaxial compression. Figure 4(b) shows the relationship of concrete stress f_c after reaching $f_c^{'}$ and the displacement Δ due to the inelastic deformations developed in a part of the element length along the axis of the element. The area under the f_c-Δ diagram is defined as the fracture energy G_f of concrete in compression. Experimental work has shown that G_f has small dependence on the length of the element, and the majority of Δ is developed over a small region. Thus, the stress versus average strain along the length of the element, L, is shown in Figure 4(c). Since G_f is a material constant, the ultimate strain ε_u is determined based on the element length L.

The effect of element length is also accounted for in determining the β-ε_n relation with $\varepsilon_{int} = (600/L_g)\cdot 1\%$ and $\varepsilon_{res} = (600/L_g)\cdot 2.5\%$, where L_g is the average length of gauge elements g_1 and g_2 shown in Figure 3(a).

For the truss elements used in the model, L is the length of each truss element. To determine the stress-strain relationship of concrete used in the beam elements, a different stress-strain is assigned for each integration point, which is adjusted based on the weighted length corresponding to the integration point as proposed by Coleman and Spacone (2001). For example, for an element of length L with four integration points, the weighted length of the end and middle integration points is $L / 12$, and $5L / 12$, respectively. Values of ε_u, ε_{int}, and ε_{res} used in the case studies presented below are listed in Table 1.

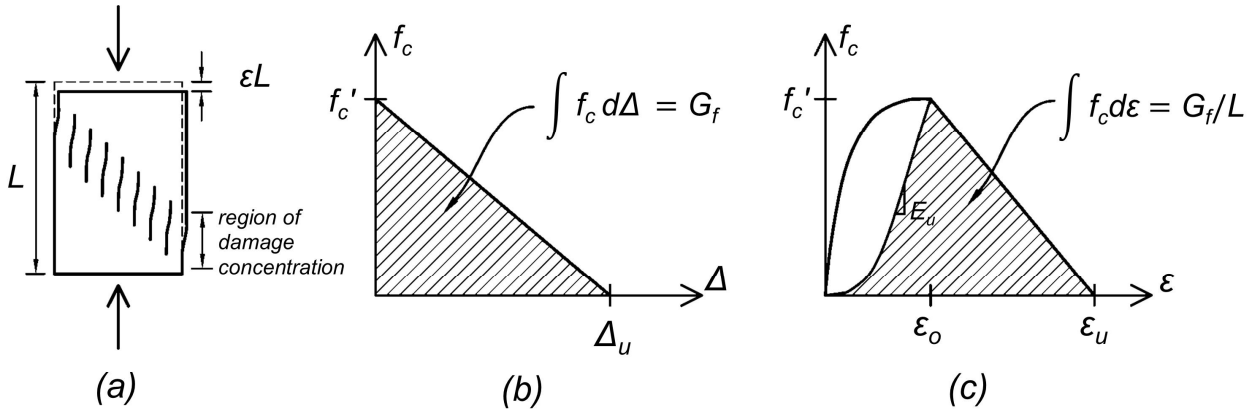

Figure 4. (a) Localization of damage in a concrete element subjected to uni-axial compression; (b) Compressive stress versus Δ, the inelastic axial displacement within the region of damage concentration after reaching f_c', and definition of concrete fracture energy in compression; and (c) average stress-strain behavior of concrete element of length L in compression and definition of fracture energy normalized to element length.

Table 1. Values of characteristic compressive strains of concrete accounting for size effects in the beam and truss elements of the different models.

	reference length L_R = 600 mm	TW2-9	TUB-11	F1-11
ε_u (beam)	0.4%	1.89%	1.75%	1.51%
ε_u (truss)	0.4%	0.66%	0.60%	0.55%
ε_{int}	1.0%	1.7%	1.52%	1.43%
ε_{res}	2.5%	4.25%	3.8%	3.58%

Reinforcing Steel

The Giuffré-Menegotto-Pinto model (GMP) was used to model reinforcing steel. The stress-strain relation is shown in Figure 5, where E_s = 200 GPa is the initial elastic modulus, f_y is the yield strength, and B_s is the post-yield hardening ratio. The parameters controlling the transition between the elastic to plastic branches (Filippou et al. 1983) were: R_0 = 18, cR_1 = 0.925, and cR_2 = 0.15 for all case studies. The effect of geometric nonlinearity (bar buckling) is not considered in this study.

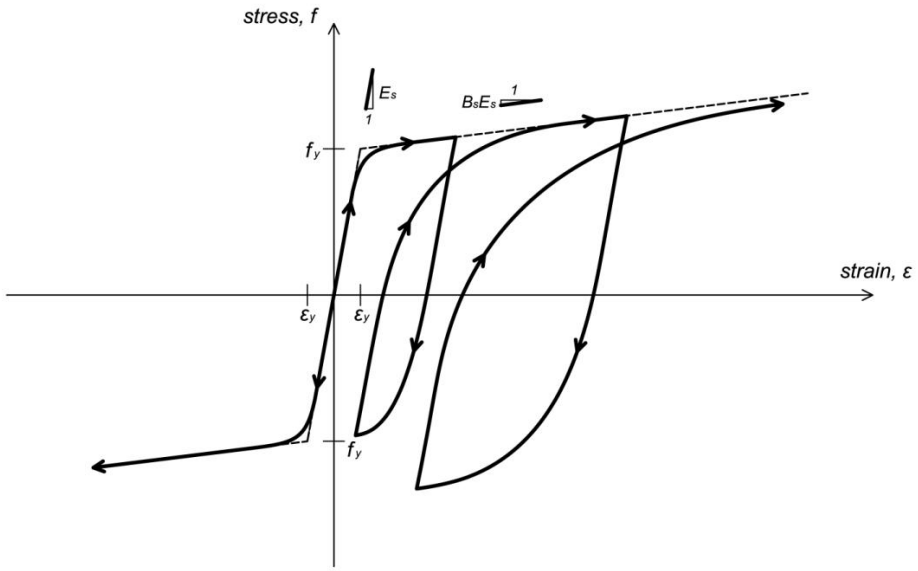

Figure 5. Stress-strain relationship of steel material model.

Computer Program Used and Implementation

The model described in this report was implemented in the computer program OpenSees (McKenna et al. 2000). The existing in Opensees GMP model, Steel02, was used for the reinforcing steel. The concrete models used in the beams and trusses, respectively, were implemented into the program by the authors. For the beam elements, the existing Opensees nonlinear force-based beam-column elements were used with linear geometric transformation. The Gauss-Lobatto quadrature with two or four integration points was used for the beam elements. The effect of number of integration points is discussed in section *Effect of Number of Integration Points*. The four-node truss element with linear geometry used for the diagonals was programmed in Opensees by the authors.

The response was computed using a displacement control algorithm. The details of the loading set up are described in each case study below. For case studies 1 and 3, uni-axial loading and static displacement control analysis was conducted. For case study 2, which involved bi-axial loading, the analysis was performed by controlling three degrees of freedom through pseudo-static multiple-support ground excitation.

Six Newton-Raphson iterations were followed by 1000 iterations of Newton with Initial Tangent were used in the solution algorithms. For each iteration, the residual of error was computed using Energy Increment, and the relative tolerance was equal to 10^{-5}. For case studies 1 and 3, a time step of 0.051 mm/step was used. For case study 2, the loading rate was 0.25 mm/sec. Translational and rotatory masses were assigned to all nodes, resulting in a first mode period of the model equal to 0.1 sec. This analysis was conducted at a time step of 0.125 sec/step.

Model Validation

Case Study 1 – Thomsen and Wallace (1995 and 2004) – Specimen TW2

In this case study, a T-shape section RC wall, called TW2, was considered (see Figure 6). The shear span ratio was $M/VL_w = 3$, where M is the bending moment at the base of the wall, V the base shear force, and L_w the length of the wall in the direction of loading. The length of both the web and the flange of this wall was 1219 mm. The axial load ratio of the wall was $N / f_c^{'} A_g = 0.074$ where N is the vertical load applied at the centroid of the section and A_g is the gross T-shape section area. The vertical load remained constant during the cyclic load reversals. The lateral and vertical load was applied through a steel beam that was placed at the top of the web in the direction of loading. The longitudinal and transverse reinforcing steel ratios, ρ_l and ρ_t, respectively, were equal in each of the two segments of the

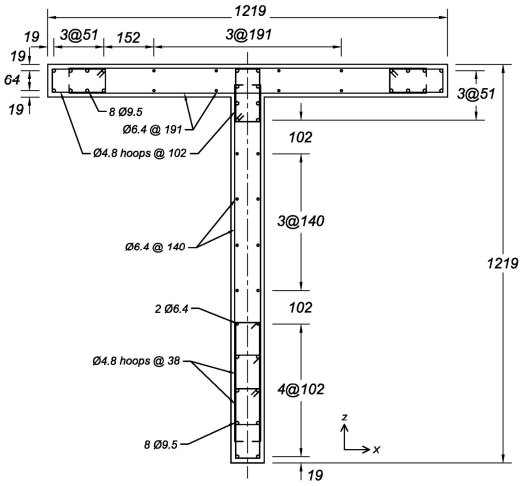

(a) Section reinforcing details of specimen

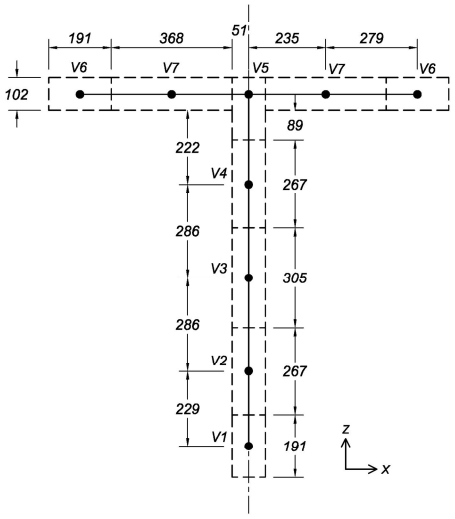

(b) Plan view of TW2-9

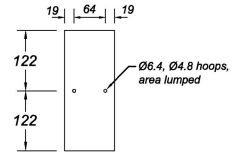

(c) Horizontal element details

dimensions in mm

material properties:

Reinforcing Steel:

	Ø9.5	Ø6.4	Ø4.8
f_y (MPa)	434	448	448
f_u (MPa)	641	586	483
ε_{sh}	1.6%	-	-
ε_{su}	10.0%	8.0%	6.0%

Concrete:

f_c' (MPa)	41.4
ε_o	0.2%
f_t (MPa)	2.13

Confined Concrete:

	V1,V2	V5	V6,V9
f_{cc} (MPa)	57.9	43.4	49.6
ε_{co}	0.6%	0.25%	0.40%
ε_{cs}	1.48%	0.71%	1.04%

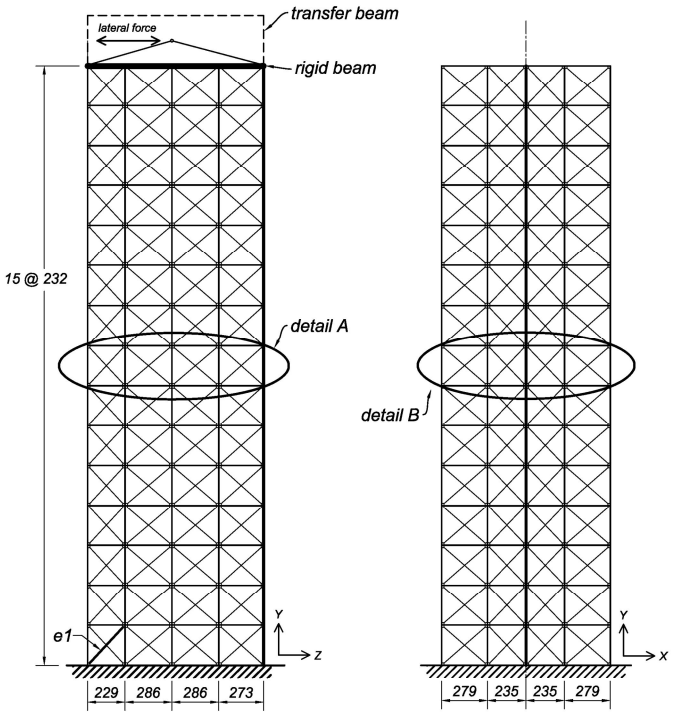

(d) Elevation view of TW2-9

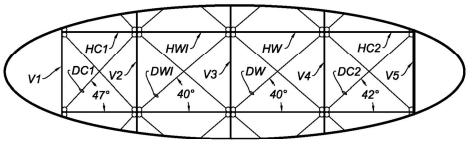

(e) Detail A

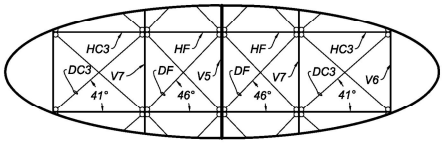

(f) Detail B

Horizontal steel areas:

	As (#2)	As (3/16")
HC1:	110.3 mm²	273.5 mm²
HWI:	110.3 mm²	45.8 mm²
HW:	110.3 mm²	-
HC2:	110.3 mm²	34.2 mm²
HF:	81.3 mm²	-
HC3:	81.3 mm²	34.2 mm²

Diagonal areas:

A_{DC1}:	102x176 mm²
A_{DWI}:	102x181 mm²
A_{DW}:	102x178 mm²
A_{DC2}:	102x181 mm²
A_{DF}:	102x177 mm²
A_{DC2}:	102x177 mm²

Figure 6. Case study 1 – TW2: Description of the specimen and TW2-9 beam-truss model.

wall. The steel ratios were equal to 0.45% in the web and 0.33% in the flange. The volumetric confinement ratio in the boundary elements, ρ_v, at the end of the web was equal to 1.31% in the plane and 0.61% out of the plane. The volumetric confinement ratio was 0.57% at the end of the flanges and 0.43% at the intersection between the flange and web. The ratio between the spacing of the transverse reinforcement of the boundary elements, s, and longitudinal bar diameter, d_b, was s/d_b = 4.0 at the end of the web, 10.7 at the intersection, and 8.0 at the ends of the flange.

Figure 7(a) shows the experimentally measured lateral force versus lateral displacement response of TW2. Positive displacement is in the direction in which the flange is in compression, and negative displacement is the direction in which the flange is in tension. The response was highly non-symmetric due to the non-symmetric shape of the section and distribution of the longitudinal reinforcement. The specimen was tested in both directions up to drift ratio $\Theta = 2.5\%$. The drift ratio is defined as Δ / H, where Δ is the lateral displacement, and H is the height where the lateral load is applied. At the first cycle of peak drift ratio, $\Theta = 1.5\%$, spalling of the cover concrete was observed at the end of web at the base of the specimen. The specimen experienced lateral strength degradation during the second and third cycles, at peak drift ratio $\Theta = 2.5\%$ for the direction of the response with the flange in tension due to extensive spalling and out-of-plane buckling of the confined core of the boundary region at the end of the web. The profile of tensile strains along the flange for the direction of loading where the flange is in tension is shown in Figure 8. The strain profiles were more uniform for drift ratios up to 1.5%, while larger strains concentrate near the mid-length of the flange was observed for drift ratios of 2% and 2.5%. The experimentally measured compressive strain at the end of the web using a 229-mm-long displacement transducer was 0.52% and 1.04% at Θ = 1.0% and 1.5%, respectively.

Three numerical models were developed for this case study. The first two were beam-truss models (BTM), shown in Figures 6 and 9, respectively, while the third was a model using only fiber-section Euler Bernoulli beam elements, referred to as the "beam model" from now on. To investigate the effect of mesh refinement on the computed response, the two BTMs differed in the number of elements used. As shown in Figure 6(b), the first BTM, termed TW2-9, incorporated five lines of vertical beams in each of the web and the flange; thus, it had 9 nodes at its base. Horizontal beams were used every 232 mm in both the web and the flange, resulting in diagonal trusses with angles ranging from 40° to 47°, see Figure 6(e) and (f). The tables in Figure 6 list the areas used in the truss elements. An elastic beam was used at the top of the model through which the lateral displacements were imposed. The second BTM, termed TW2-17 and shown in Figure 9, used 17 vertical lines of beam elements to represent the entire T-section, resulting in almost two times finer mesh than this of TW2-9 with angles of diagonals ranging between 41° and 47°.

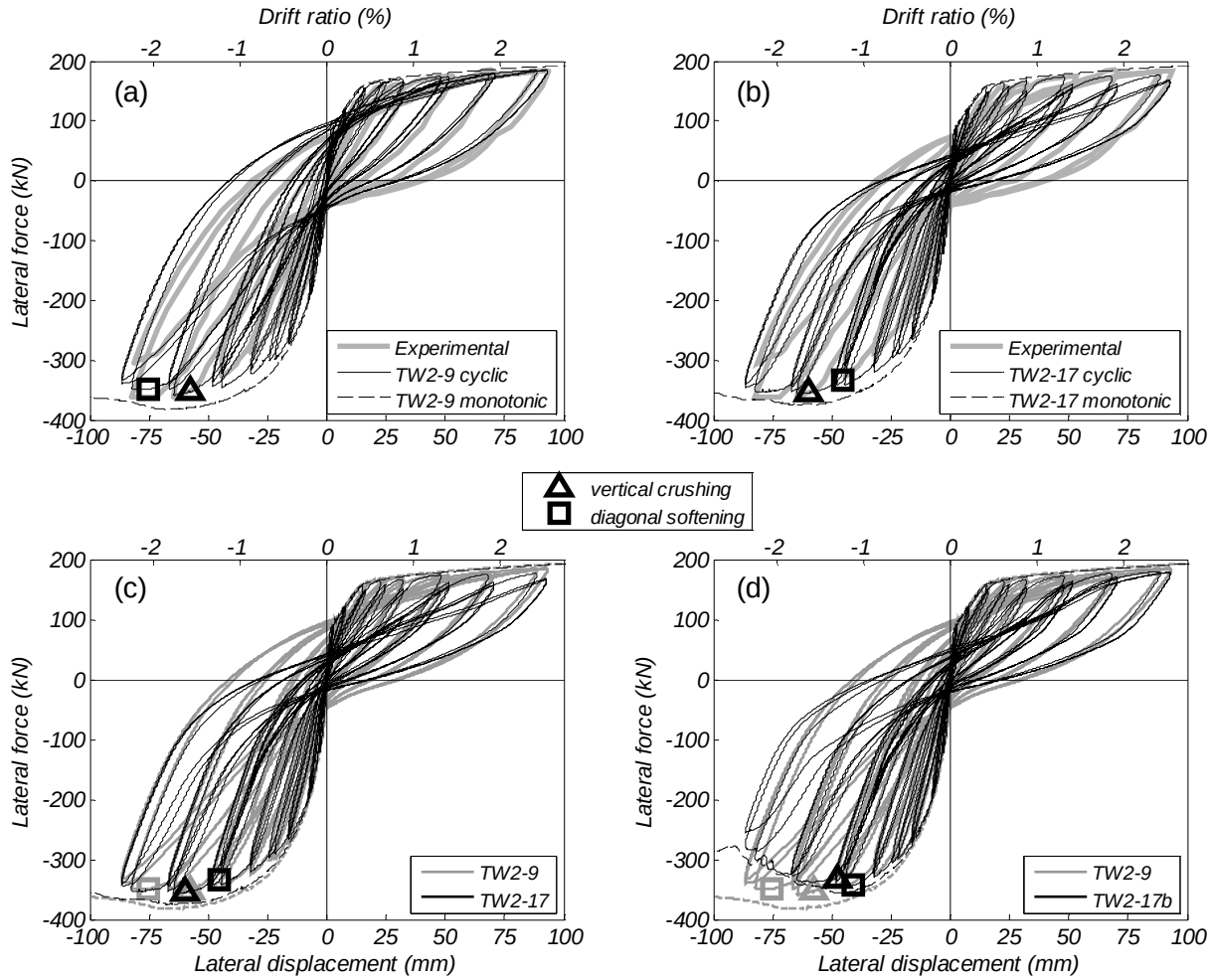

Figure 7. Case Study 1 – TW2: (a) Comparison of measured and computed response using the TW2-9 model; (b) Comparison of experimental and computed response from the TW2-17 model; (c) Comparison of computed response using the TW2-9 and TW2-17 models; and (d) Comparison of computed response using TW2-9 and TW2-17b models with the latter not accounting for size effects.

Figure 7(a) compares the experimentally measured and numerically computed response using the TW2-9 model. The numerical model computed the force-displacement response very satisfactorily. Compared to the measured experimental values, the computed peak lateral strength was in excellent agreement for the positive displacement response, and 1% smaller for negative displacement response. The model overestimates the lateral strength for positive displacement for drift ratios up to 1.5%. This is mainly due to the overlap of vertical and diagonal areas of concrete in this model. This was also observed for small drift ratios corresponding to small deformations in the 2D models of planar walls of Panagiotou et al. (2012). The computed lateral strength at $\Theta = 1.0\%$ exceeds the experimentally measured response by 13%. The overestimation of lateral strength was 6% at $\Theta = 1.5\%$. The difference between the

computed and experimentally measured lateral strength was less than 6% for drift ratios larger than 1.5%. TW2-9 computed crushing of the unconfined concrete in the vertical direction at the end of the web in the first cycle with peak drift ratio $\Theta = 2.0\%$, with 7% strength degradation computed at $\Theta = 2.5\%$. This model did not account for buckling, which was the predominant mode of failure of this wall. The peak diagonal compressive strain of the web computed for negative displacement was 0.3%, measured in element e_1 shown in Figure 6(d). This was in good agreement with the observed response in the experiment where no crushing of the diagonal compression field was observed. The comparison of the computed responses using the TW2-9 and TW2-17 models is presented in the *Effect of Mesh Refinement* section.

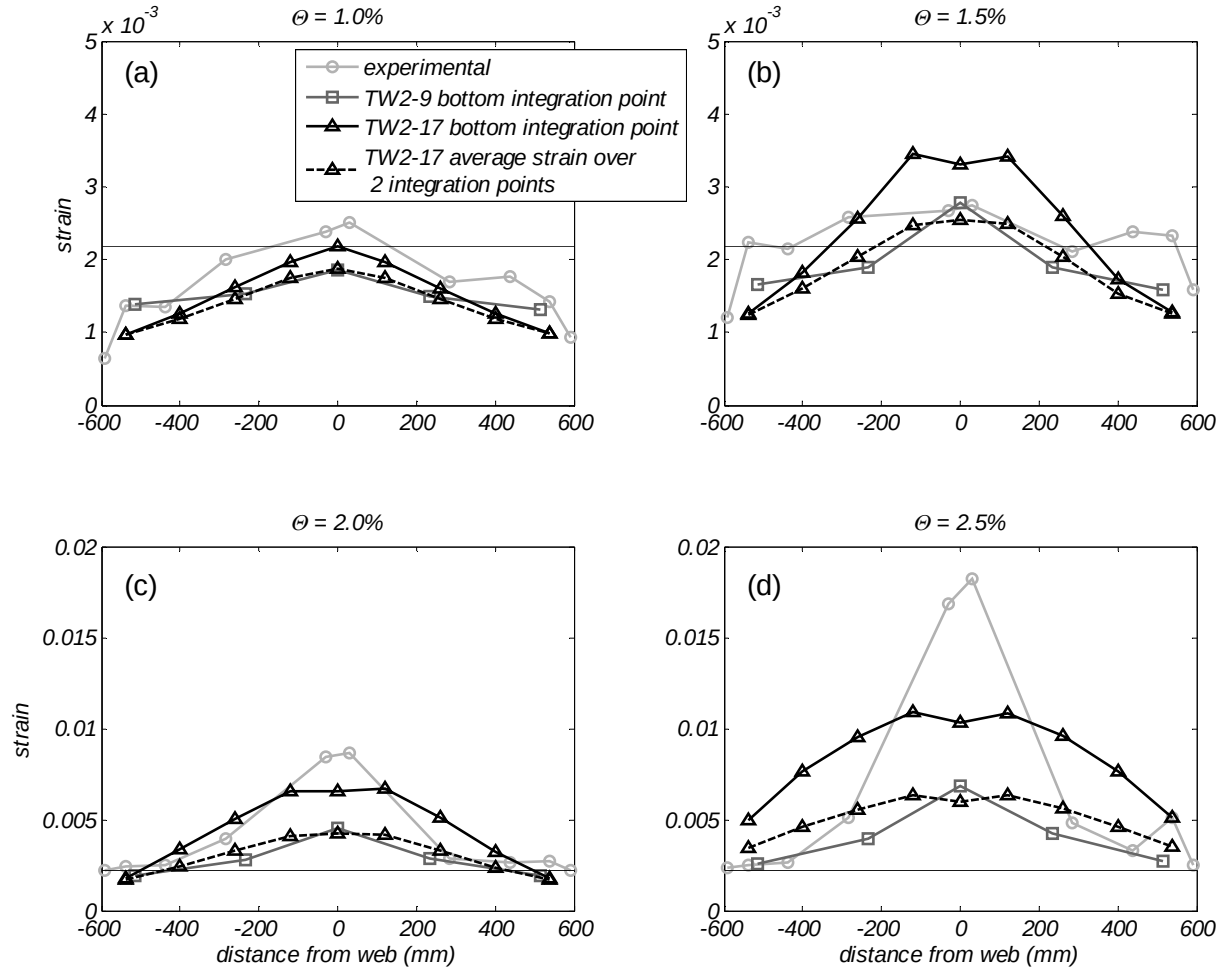

Figure 8. Case Study 1 – TW2: Comparison of measured and computed steel tensile strains along the base of the flange for drift ratios (a) 1.0%; (b) 1.5%; (c) 2.0%; and (d) 2.5%.

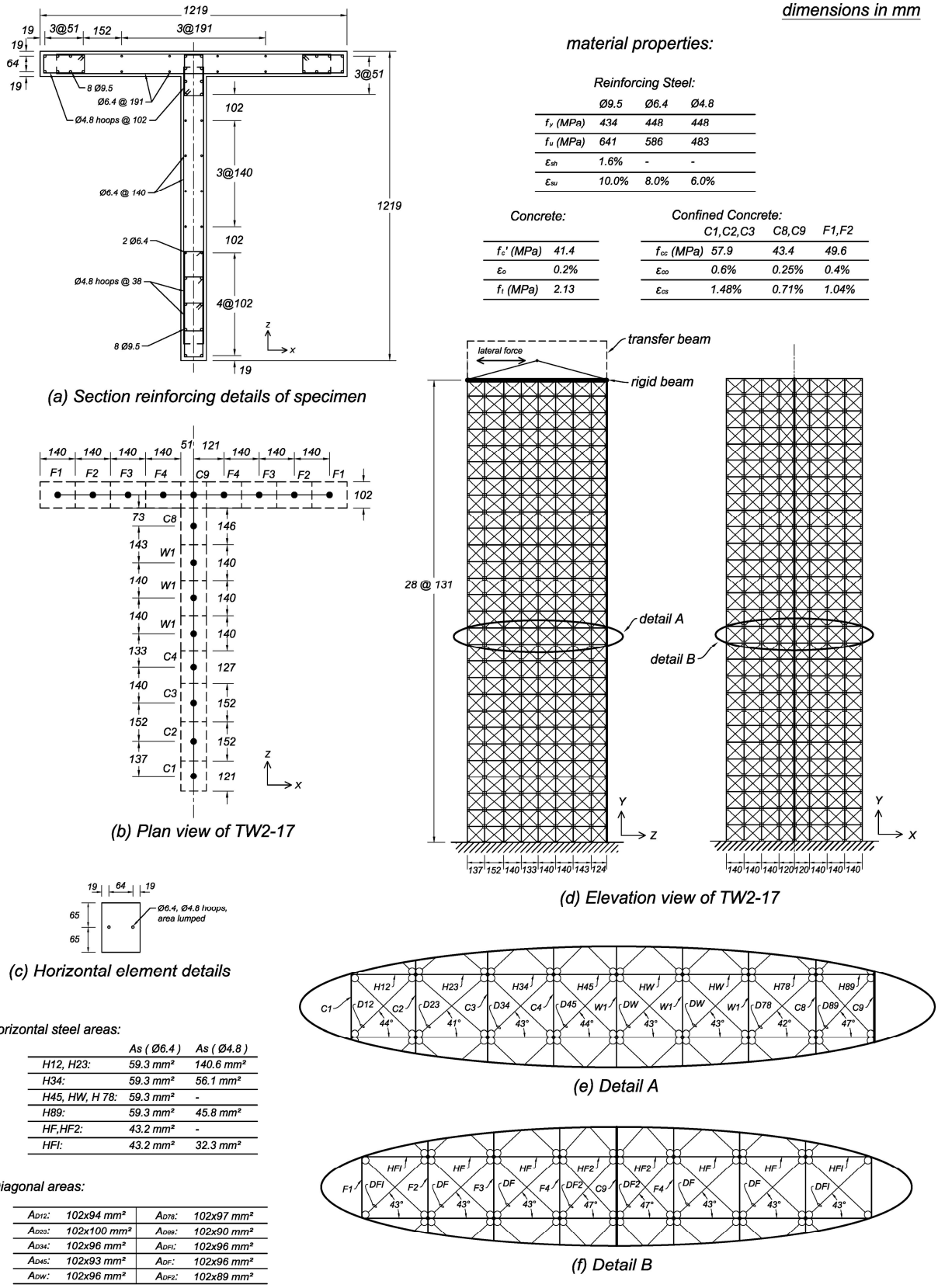

Figure 9. Case Study 1 – TW2: Description of the specimen and TW2-17 beam-truss model.

Figure 8 compares the experimentally measured and numerically computed steel tensile strain profiles along the flange near its base. Strain gauges attached on the reinforcing steel bars 51 mm above the base were used to record tensile strains. The numerically computed strains at the bottom integration point correspond to an average strain over 232 mm. For $\Theta \leq 1.5\%$, the computed strains were in good agreement with the measured strain profile. For $\Theta \geq 2.0\%$, the computed strains using TW2-9 were in good agreement at the ends of the flange, but there was more than 50% underestimation of the tensile strains at the middle of the flange. The numerically computed compressive strain at the end of the web for TW2-9 was -0.43%, and -0.72% at $\Theta = 1.0\%$ and 1.5%, respectively, and were in good agreement with the experimentally measured strains of -0.52% and -1.04%, respectively. The computed strain does not account for the effects of bond slip. The differences in computed strain profile between the coarser-mesh TW2-9 model and the finer-mesh TW2-17 model are discussed in the *Effect of Mesh Refinement* section.

Figure 10(a) shows the comparison between the experimentally measured response and the computed response using the beam model, TW2-B2ip, which had elements of length equal to that of the vertical elements of the BTM TW2-9 and used two integration points per element. The beam model resulted in poor prediction of the response for negative displacement and overestimated the strength at $\Theta = 1.0\%$ by 35%. In addition, the calculated peak lateral strength occurred at $\Theta = 1.0\%$ and was 6.7% larger than the experimentally measured peak strength, which occurred at $\Theta = 2.5\%$. This was due to the uniform strain along the flange imposed by the plane-section-remain-plane assumption in the beam elements. Compared to the experimental response, the computed response showed a sudden loss of strength in the first cycle at peak drift ratio $\Theta = 2.0\%$, which was due to the higher contribution of flange in tension, resulting in a significantly larger compression force at the end of the web and crushing of the concrete. In the case of flange in compression, the computed response was in better agreement with the measured response in terms of lateral strength, but it computed higher unloading stiffness.

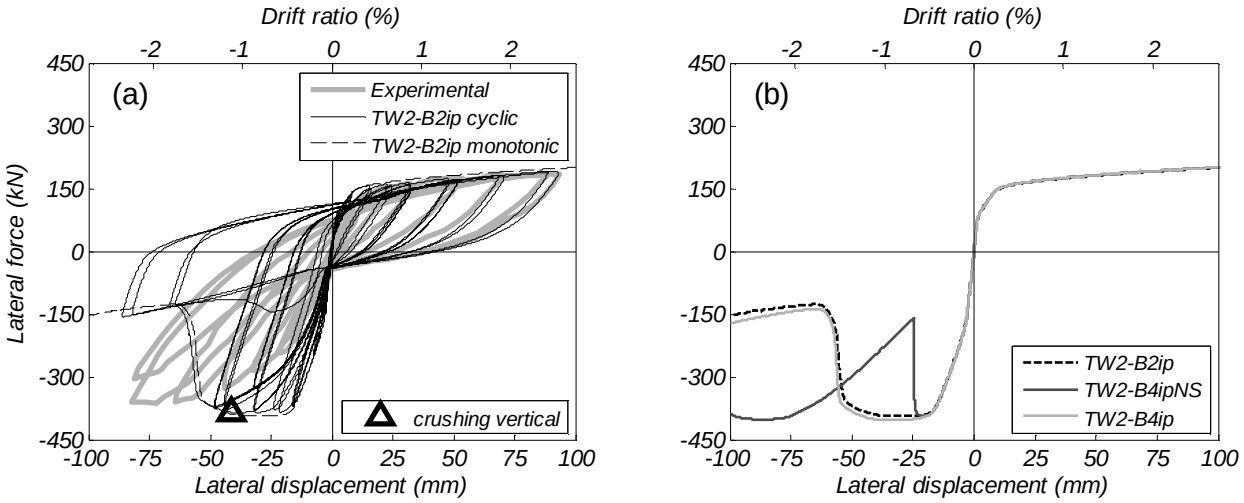

Figure 10. Case Study 1 – TW2: (a) Comparison of measured and computed, using beam model TW2-B2ip, responses; and (b) Comparison of monotonic responses of the beam models TW2-B2ip, TW2-B4ip, and TW2-B4ipNS, which did not account for size effects.

Case Study 2 – Beyer et al. (2008a) – Specimen TUB

The test specimen of Case Study 2, called TUB, was a U-shape section wall with M/VL_w = 2.8 in the E-W direction and 2.6 in the N-S direction, see Figure 11. The length of this wall in the N-S and E-W direction was 1050 and 1300 mm, respectively, and the axial load ratio was $N/f_c^{'}A_g = 0.04$. The axial load remained constant during the cyclic load reversals and was applied through a steel beam parallel to the EW direction, passing from the centroid of the section. To apply the lateral load, a 300-mm-thick collar was used at the top of the wall with the actuators attached to it. Three actuators were used for the experimental test, one in the E-W direction and two in the N-S direction. In all parts of the wall, the reinforcing steel ratios ρ_l and ρ_t were equal to 0.38% and 0.45%, respectively. Boundary elements were used at the ends of each of the three segments of the wall, see Figure 11(c). For the boundary elements at the south end of the wall, the volumetric confinement, ρ_v, was equal to 1.66%, and 0.85% in the N-S and E-W direction, respectively. At the intersections of the wall segments, ρ_v was equal to 1.46%. The ratio s/d_b was equal to 4.2.

The experimentally measured force-displacement response of TUB is shown in Figure 12. At each level of lateral displacement, the specimen was tested with one cycle in each of the E-W, N-S, and diagonal (SW – NE) directions as well as a sweep cycle resembling an hourglass shape in top view (Beyer et al. 2008). The recorded force-displacement responses are plotted separately in each of the E-W and N-S

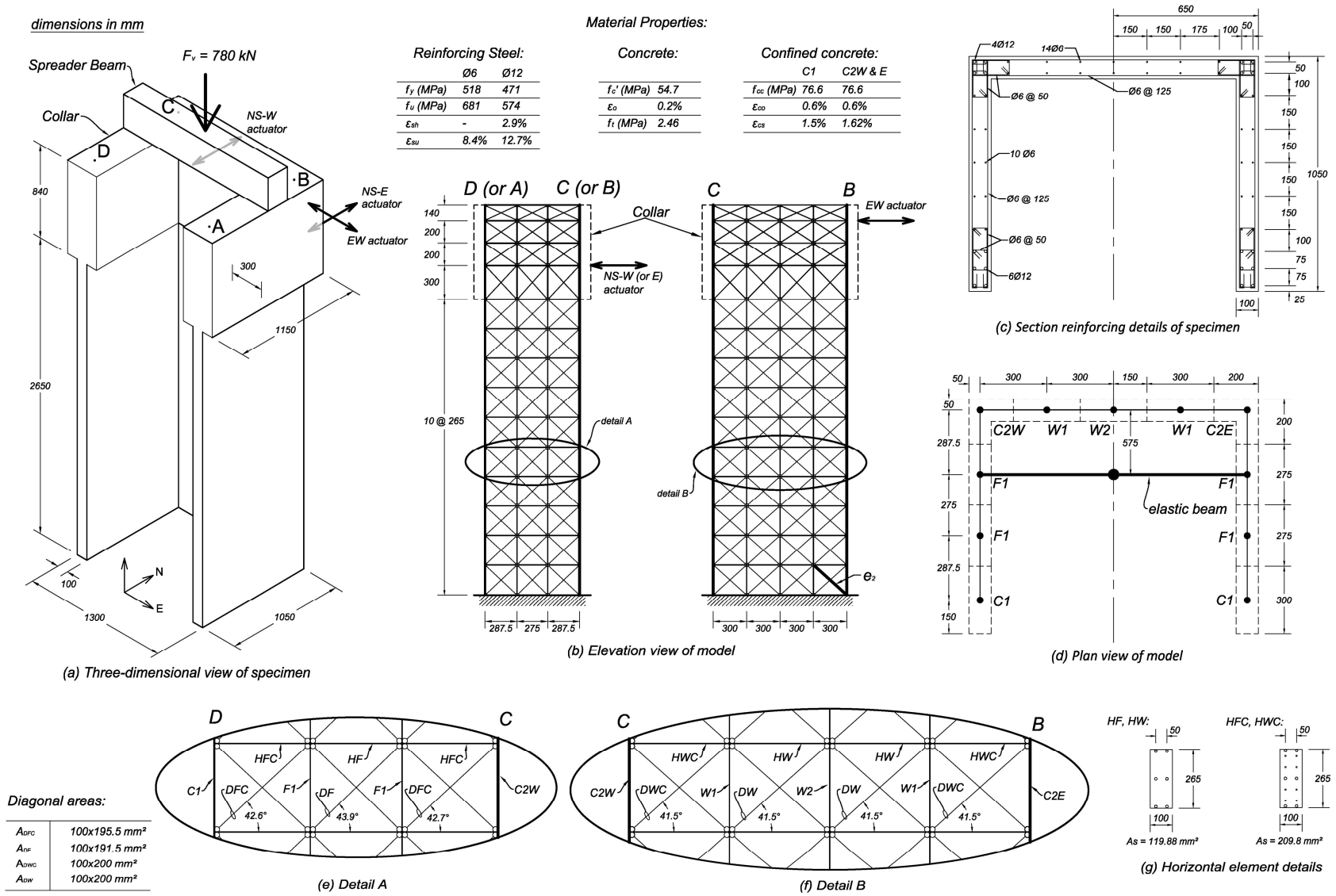

Figure 11. Case Study 2 – TUB: Description of specimen and TUB-11 beam-truss model.

directions for each type of loading cycle. The specimen was tested up to drift ratios of $\Theta = 3\%$ in all directions. The response of the E-W cycles was nearly symmetric, while the response of the N-S cycles was slightly asymmetric as were the responses in the diagonal and sweep cycles. Spalling of the boundary elements began at a drift ratio of 1% for loading in the N-S direction and spread to the regions without boundary elements. The specimen failed due to crushing of concrete compression diagonals at about 260 mm from the base of the segment of the wall parallel to the E-W direction during the sweep cycle at peak drift ratio $\Theta = 3\%$. The peak lateral force in the E-W direction was $5.4A_w\sqrt{f_c'}$, where A_w is the total cross-sectional area of segment of the wall parallel to the EW direction, and f_c' in psi. This is only 54% of the peak shear force that ACI (2011) allows.

For this case study, two numerical models were developed: a BTM and a beam model. Figure 11 shows the BTM, termed TUB-11, with four lines of vertical elements for each of the segments of the wall in the N-S direction and five lines for the third segment resulting in eleven lines of vertical elements in total. The section areas of the vertical elements are shown in Figure 11(d). The horizontal beams were placed every 265 mm, resulting in θ_g ranging from 41° to 44°. The collar was also modeled with a BTM, see Figure 11(b). The horizontal elements were positioned to allow the application of lateral load at the same height as in the experiment. An elastic beam was placed at the top of the collar to model the steel spreader beam, see Figure 11(d).

For the N-S and E-W cycles, the computed response using TUB-11 was in excellent agreement with the measured response, see Figure 12. The computed response overestimated the peak lateral force by 8.3% for the N-S cycles and underestimated by 2.7% for the E-W cycles. In the diagonal and sweep cycles, the peak lateral forces in the N-S direction were overestimated by 20% and 16%, respectively. The peak lateral forces in the E-W direction were underestimated by 6.4% and 2%, respectively. Overall, the cyclic computed response was in very good agreement with the experimentally measured for all cycles. In very good agreement with the experimentally observed diagonal crushing, the model computed crushing of the concrete 265 mm from the base at element e_2, see Figure 11 (b), in the segment of the wall parallel to the EW direction during the sweep cycle at drift ratio $\Theta = 3\%$.

However, the beam model overestimated the peak lateral force in the E-W direction by 22%, 44%, and 24% during the E-W, diagonal, and sweep cycles, respectively, as shown in Figure 13. The model did not compute significant softening of confined concrete. The significant strength degradation observed at almost every cycle of the sweep cycles was due to the change of angle of loading during the sweep cycles. Due to its inherent inability to compute the stress and strain state in horizontal and diagonal directions, this model was not able to compute crushing of the concrete in the diagonal direction, which was the failure mode of this specimen.

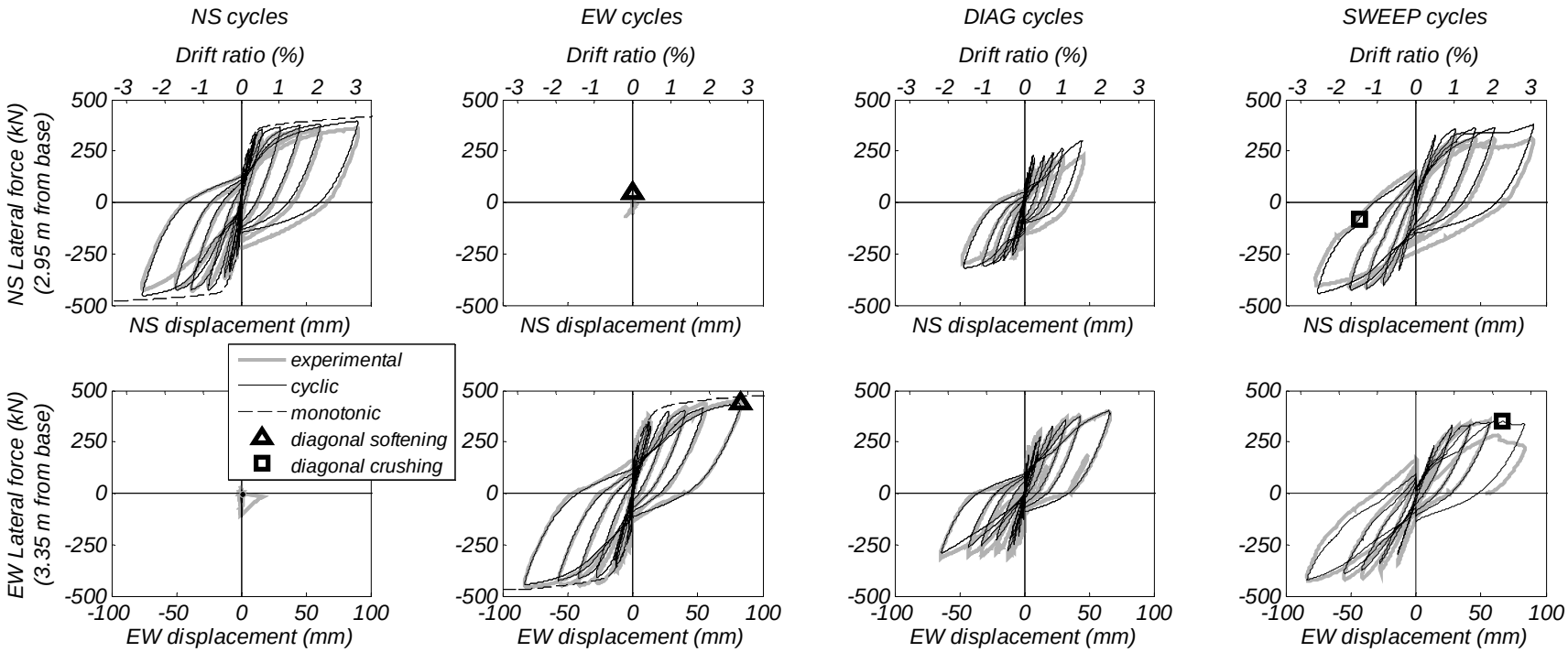

Figure 12. Case Study 2 – TUB: Comparison of measured and computed response using the TUB-11 beam-truss model.

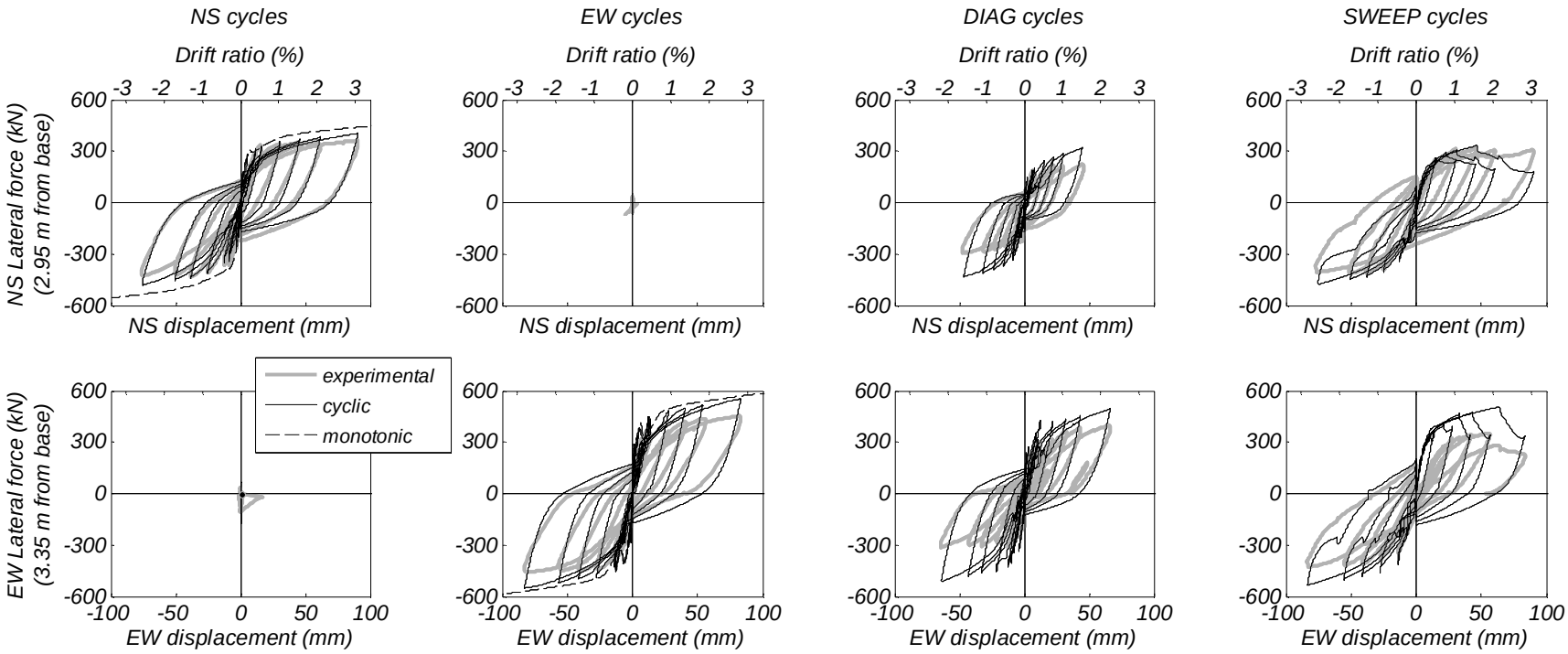

Figure 13. Case Study 2 – TUB: Comparison of measured and computed response using fiber-section beam model.

Case Study 3 – Oesterle et al. (1976) – Specimen F1

Case study 3 considered the I-shape section wall with $M/VL_w = 2.4$ shown in Figure 14(a) and (b). The two parallel segments of this wall (termed flanges) were 914 mm long, while the third segment perpendicular to them (termed the web) was 1905 mm long. The specimen was subjected to uni-axial load reversals in the direction of the web. A 203-mm-thick slab was cast at the top of the specimen. No axial load was applied on the specimen. Two actuators applied lateral load at 4572mm from the base of the wall, passing through the centroid of the web. The longitudinal steel ratio in the flanges and the web was 3.9%, and 0.24%, respectively. The transverse steel ratio was 0.63% both in the web and the flange. The volumetric ratio of confinement reinforcement of the flange was 0.28% and 1.12% in the direction parallel and perpendicular to the flange, respectively. The ratio between the spacing of the confinement transverse reinforcement in the flange s and the longitudinal bar diameter d_b was s/d_b = 7.0.

Figure 15(a) shows the experimentally measured force-displacement response of F1. The specimen was tested up to $\Theta = 2.2\%$ with 3 cycles at each level of displacement. Spalling in the diagonal direction was first observed during the second cycle at 1.1% peak drift ratio. The specimen experienced significant loss of the lateral strength during the first cycle of 2.2% drift ratio due to crushing of concrete of the web in the diagonal direction at 300 mm from the base of the wall. The peak lateral strength of this specimen was $8.6A_w\sqrt{f_c'}$, where A_w is the total section area of the web.

Four numerical models were developed. Three of them were beam-truss models, and one is a beam model. The first two BTMs had eleven lines of vertical beams, see Figure 14(c). The first BTM (termed F1-11-45) had horizontal beams every 298 mm, resulting in θ_g ranging from 44° to 46°, see Figure 14(d). The second BTM (termed F1-11-45) had horizontal beams every 373 mm, resulting in θ_g around 50°, see Figure 14(h). The third BTM (termed F1-19-45) had almost two times more refined mesh than that of F1-11-45, and had nineteen lines of vertical beams and horizontal beams every 179 mm, resulting in θ_g around 45°, as shown in Figure 16. The top slab of each BTM was modeled with an elastic beam element.

Figure 15(a) compares the experimentally measured and numerically computed response using the F1-11-45 model. The computed response was in very good agreement with the experimental response in terms of peak strength and the general hysteretic response. The BTM underestimated the peak lateral strength by 5%. The model, in very good agreement to the experimentally observed response, computed diagonal crushing of concrete at the first cycle with peak drift ratio $\Theta = 2.2\%$ in the diagonal truss element, e_3, at the base of the web, shown in Figure 14(d). Following the crushing of diagonal, the beam-truss model does not show as much lateral strength degradation as shown in the experimental response. The comparison of response with the BTM F1-11-50 is presented in the section *Effect of the Angle of the*

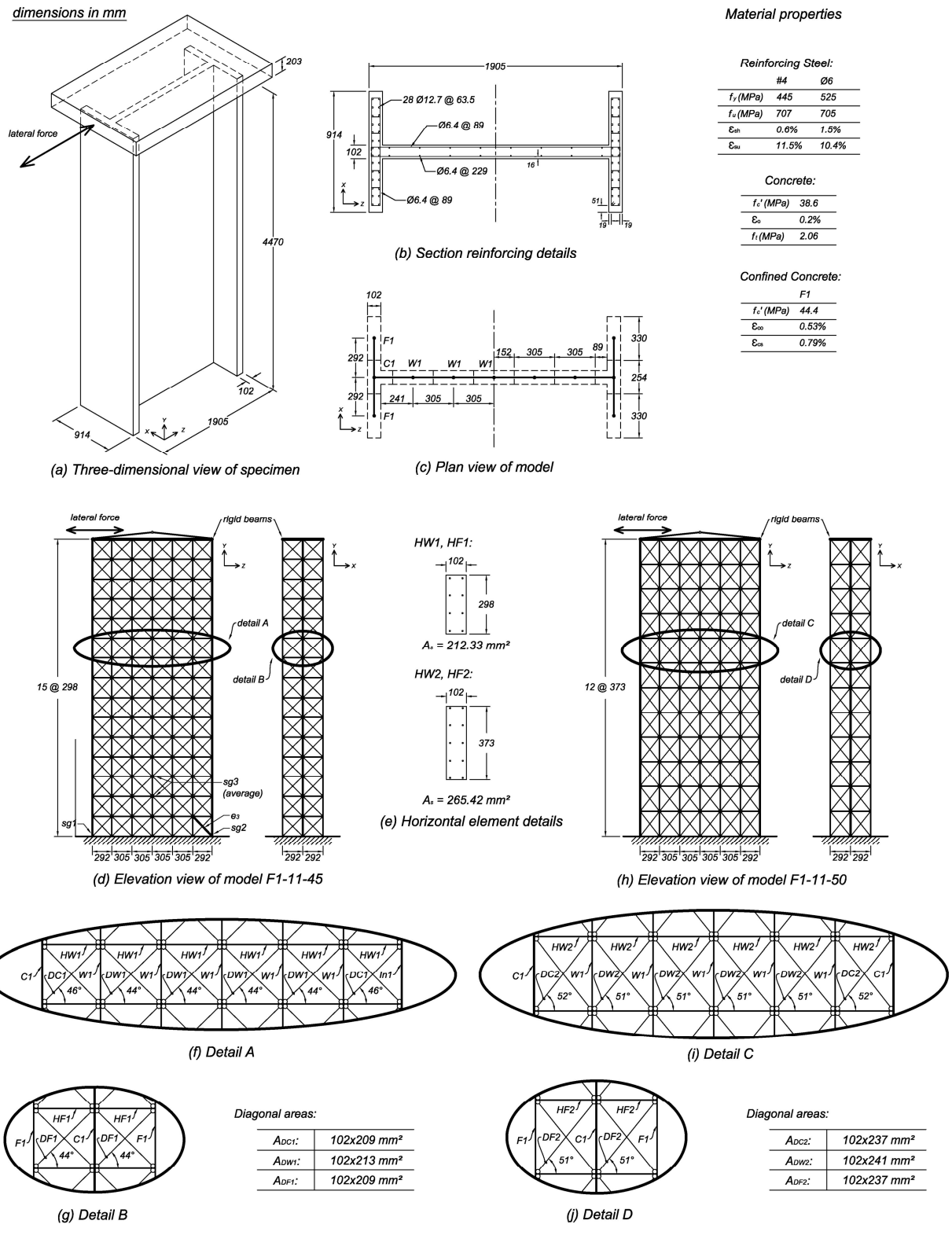

Figure 14. Case Study 3 – F1: Description of specimen and beam-truss models F1-11-45 and F1-11-50.

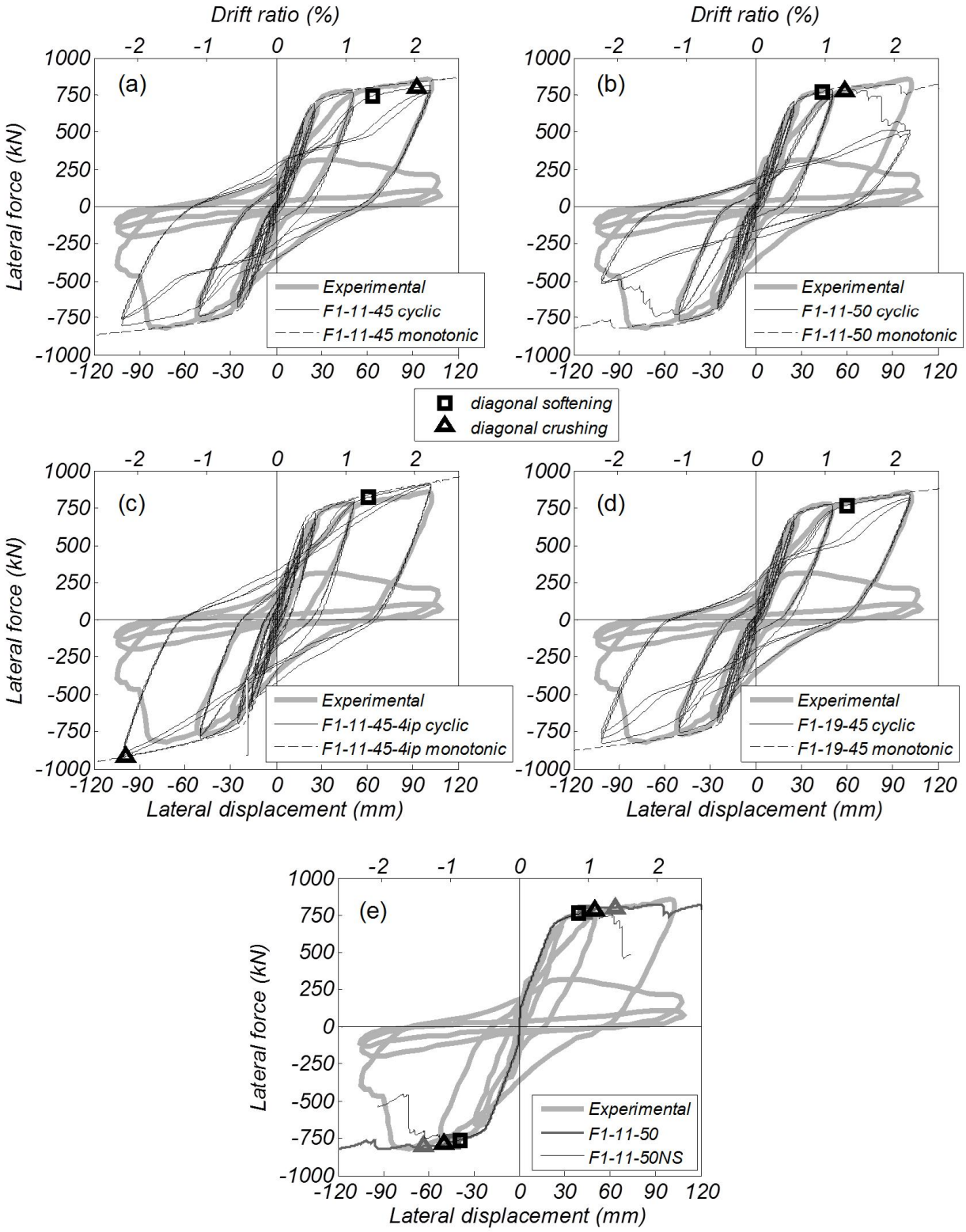

Figure 15. Case Study 3 – F1: Comparison of experimental and computed responses using (a) F1-11-45; (b) F1-11-50; (c) F1-11-45-4ip; (d) F1-19-45; and (e) comparison between computed responses using F1-11-50 and F1-11-50NS.

Diagonal Truss Elements of the discussion. Comparison of the computed responses using the F1-11-45 and F1-19-45 models is presented in the *Effect of Mesh Refinement* section. Figure 17 shows the experimentally measured response using strain gauges attached on the steel bars and computed strains, using three BTMS, versus lateral force. The response was plotted up to the first cycle of $\Theta = 2.2\%$ (where experimentally measured strain data exist). The locations of the strain gauges are shown in Figure 14(d) for the F1-11-45 model. The strains computed from this model were in fair agreement with the measured longitudinal and transverse strains at the base. For the $\Theta = 2.2\%$ cycles, the maximum computed strains at the locations of *sg1*, *sg2*, and *sg3* were 55% smaller, 61% smaller, and 10% larger than the measured strains, respectively. This was partially because the model does not account for bond slip and because the computed strains were smeared over the length of the element and did not account for effects of strain localization that may have occurred in the experimental response. The effective length over which the strains were computed was 149 mm for *sg1* and *sg2*, and 153 mm for *sg3*. The effect of using four integration points for the computed strain values is discussed in the *Effect of Number of Integration Points* section while the strains computed using the F1-19-45 model is discussed in the section *Effect of Mesh Refinement*.

The comparison of the experimentally measured and numerically computed responses using a beam model, termed F1-B2ip with elements of length equal to that of the vertical elements of BTM F1-11-45, is presented in Figure 18(a). The model overestimated the peak strength of the specimen by 20%. The computed hysteretic behavior demonstrated that the shape of the computed response was governed by the large amount of reinforcing steel in the flanges and their hysteretic behavior. This resulted in significantly higher hysteretic energy dissipation per cycle than the measured response. The beam model, due to its fundamental limitation, did not calculate the inelastic strains of the horizontal reinforcement as well as the crushing of the concrete diagonals, which was the governing failure mode of this specimen.

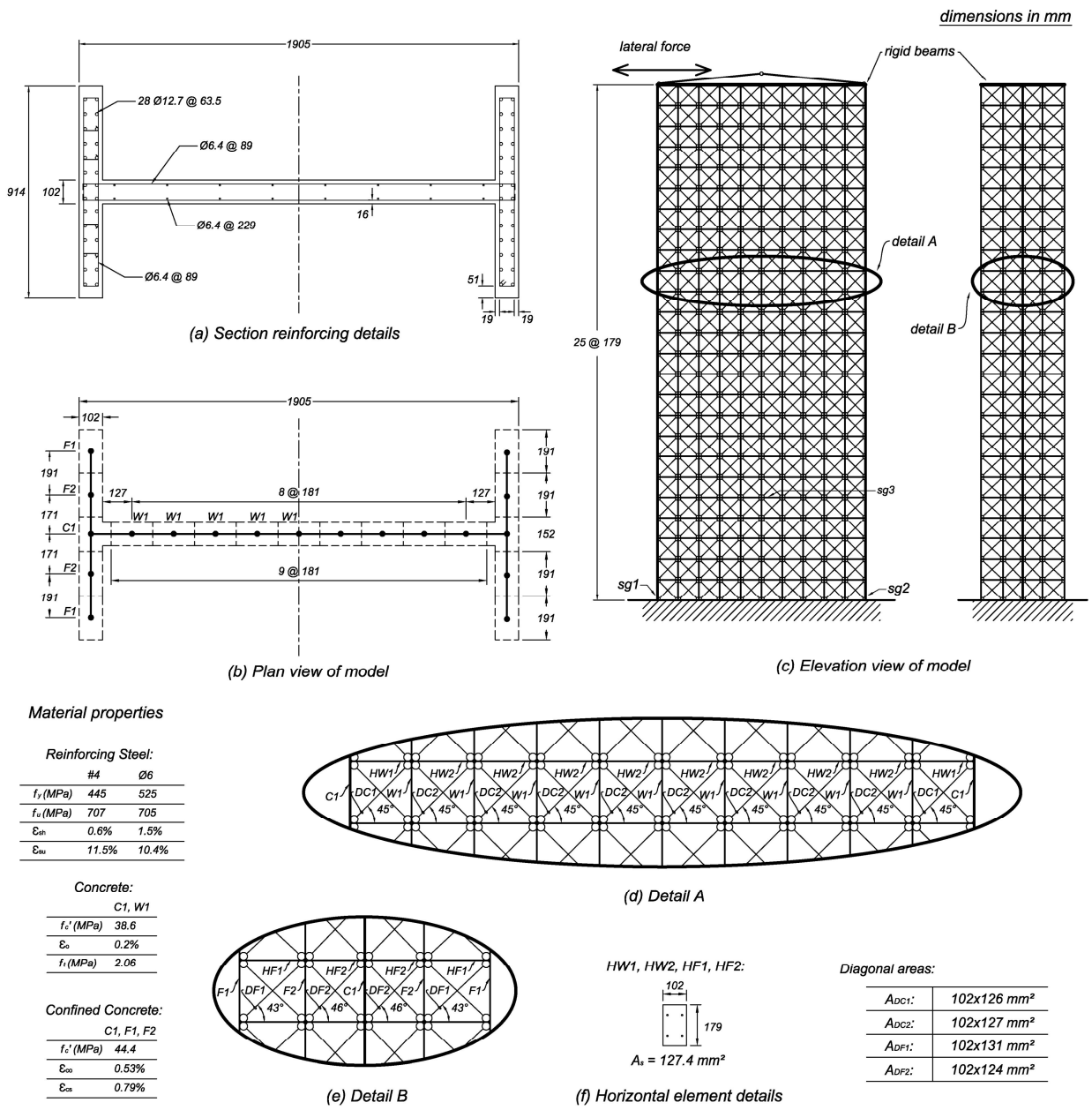

Figure 16. Case Study 3 – F1: Description of refined beam-truss model F1-19-45.

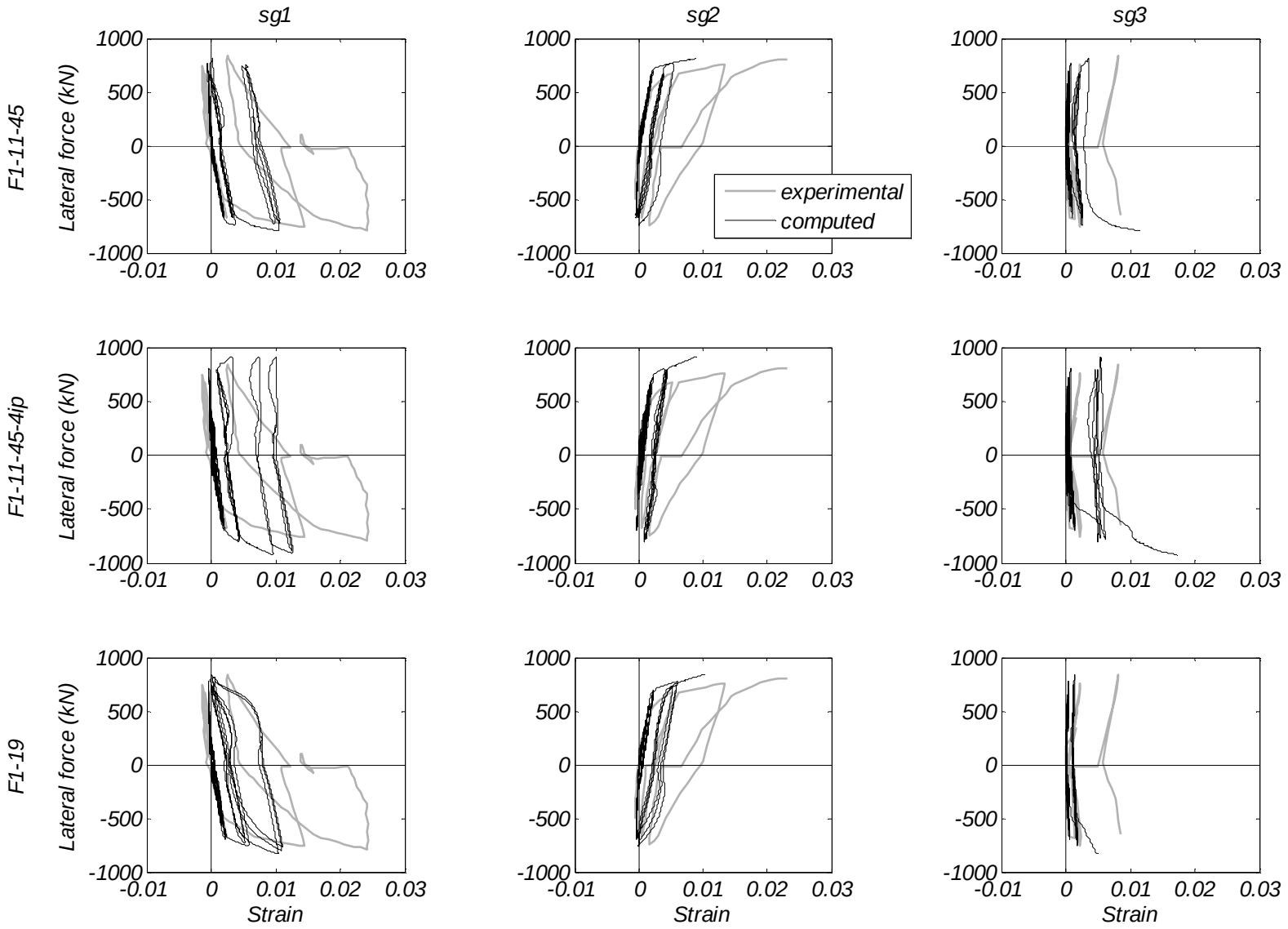

Figure 17. Case Study 3 – F1: Comparison of measured and computed lateral force versus strain using models F1-11-45, F1-11-45-4ip, and F1-19-45. The locations of all strain gauges *sg1*, *sg2*, *sg3* are shown in Figure 14 and Figure 16 for BTMs F1-11-45 and F1-19-45 respectively.

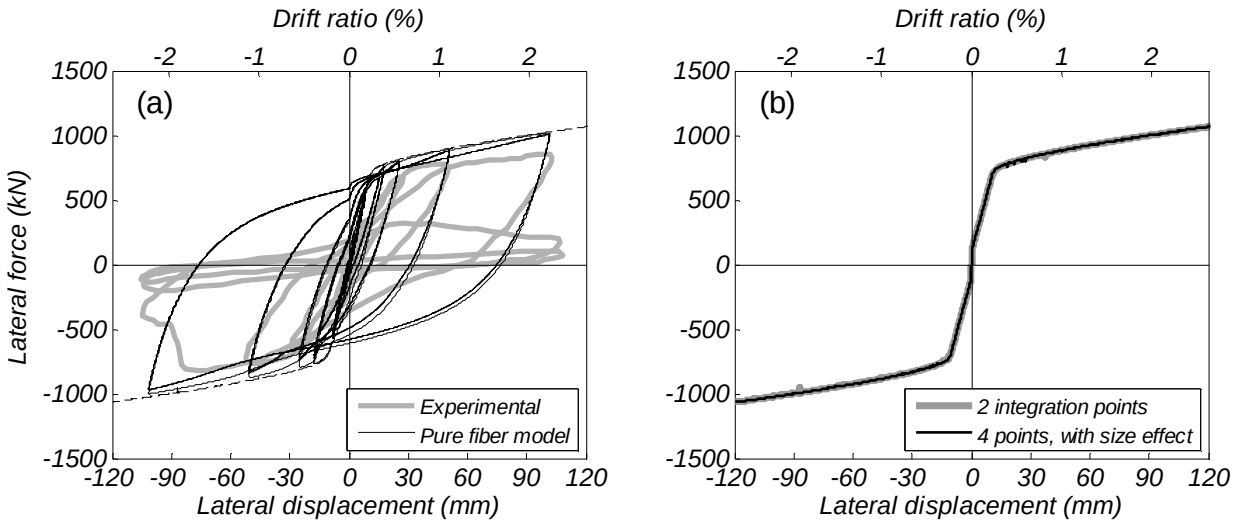

Figure 18. Case Study 3 – F1: (a) Comparison of measured and computed response using beam model F1-B2ip; and (b) Comparison of monotonic response using beam models F1-B2ip and F1-B4ip.

Discussion

Comparison of the experimentally measured and numerically computed responses using the beam-truss model developed in this study demonstrated that the latter computes very satisfactorily the force-displacement of the three non-planar walls considered subjected to uni- and multi-axial cyclic load reversals. By considering the horizontal stress and strain field of steel and concrete in the horizontal directions and coupling the effect of normal strain to the compressive behavior of diagonal concrete in compression, the model captured the important effect of flexure-shear interaction in Case Studies 2 and 3, where the experimentally observed failure mode was due to diagonal crushing of concrete. The model also fairly computed strains in the vertical as well as the horizontal directions compared to the experimentally measured response.

For the nonlinear fiber-section Euler-Bernoulli beam models, the plane-sections-remain-plane assumption resulted in significant overestimation of the stiffness and strength of non-planar walls. Due to its inherent limitation to calculate strains in any direction other than the vertical, these models were not able to capture the effects of FSI or the failure mode of the Case Studies 2 and 3 specimens. The following sections investigate the effect of some parameters of the numerical models, especially the beam-truss models presented.

Effect of Mesh Refinement

The effect of mesh refinement was investigated for Case Studies 1 and 3. For each model developed in this study, Table 2 summarizes the range of the ratio of length of different elements to the length of the walls, r_L, as well as the ratio of the length of the elements to the height of the walls, r_H. The ratio r_L ranged between 9% and 38.1% while r_H was between 3.3% and 13.6%.

Figure 7(c) compares the computed force-displacement response of the TW2 specimen using the TW2-9 and TW2-17 models. The two models computed similar peak strength at each cycle. At 1.0% and 1.5% drift ratios, the lateral strength of model TW2-17 is 1.2% and 1.3% smaller than that of TW2-9, respectively, which corresponds to a 4% and 11% overestimation of the experimental results. The overall peak lateral strength of model TW2-17 is 0.3% smaller than that of TW2-9. Both models computed the first crushing of the vertical concrete at the end of the web and during the same cycle at similar displacements. The TW2-17 model, with the finer mesh, computed a more pinched response.

Figure 8 compares the experimentally measured steel strains at the bottom of the flange with the computed strains using the TW2-9 and TW2-17 models. For both of the models, the computed strains were these computed at the integration point at the base of the element. Both models used two integration points per element; thus the effective length of each integration point in TW2-17 was half of the corresponding of TW2-9 model. Figure 8 also shows the average strain over two integration points of TW2-17, so that the length over which the strains were measured was similar to that in TW2-9. For $\Theta \le 2.0\%$, the strains profiles computed by TW2-9 and TW2-17, which took the average strain of the two integration points for the second model, were similar. As expected, the strain profile of TW2-17 computed at the base integration point was larger than the corresponding strain profile using TW2-9. The computed strain at the base integration point of TW2-17 exceeded the corresponding strain of TW2-9 by about 44% for $\Theta = 2.0\%$ and 51% for $\Theta = 2.5\%$ near the mid-length of the flange, where peak strains were computed at all drift ratios. The strains near the mid-length of the flange computed at the base integration point base on TW2-17 were in better agreement with the experimentally measured response. At 2% and 2.5% drift ratio, the peak computed strain was 24% and 43% smaller than the experimentally measured response, respectively.

For Case Study 3, Figure 15(a) and (d) show the comparison of the experimentally measured and computed response using models F1-11-45 and F1-19-45 BTMs, respectively. Both models result in good agreement with the experimental response, but F1-19-45 computes significant softening of the diagonal concrete of the specimen without crushing. The peak lateral strength computed by the F1-19-45 model is 3.3% larger than that computed by the F1-11-45 model. The computed strains using model F1-19-45 are shown in Figure 16. Compared to F1-11-45, the F1-19-45 model results in slightly better agreement of the

strains with the peak strain measured. For the gauges sg1, sg2, and sg3, the strains computed by F1-19-45 are 54%, 56%, and 42% smaller than the experimentally measured strains.

Table 2. List of ranges of ratio of element length to wall length r_L and to wall height r_H.

	r_L		r_H	
	Min	max	Min	max
TW2-9	18.8%	30.8%	6.3%	10.3%
TW2-17	9.9%	16.5%	3.3%	5.5%
TUB-11	19.7%	38.1%	8.0%	13.6%
F1-11-45	15.3%	22.4%	6.5%	9.5%
F1-19-45	9.0%	13.7%	3.8%	5.9%

Mesh Objectivity

As discussed in section *Mesh Size Effects*, the softening branches of the concrete compressive stress-strain relationship depend on the length of the elements and the number of integration points. Figure 7(d) compares the computed response of the specimen of Case Study 1 using the TW2-9 and TW2-17b models. The TW2-17b model had a mesh identical to TW2-17 but used stress-strain relationships for concrete in compression identical to these used in TW2-9 model. The TW2-17b model computed crushing of the vertical concrete at a displacement level 21% smaller than that computed by the TW2-9 and TW2-17 models. The TW2-17b model also resulted in a 27% decrease of strength after the computation of crushing as compared to 7% computed by TW2-9; The TW2-17b model computed 2.2 times greater strength degradation following the first vertical crushing compared to TW2-9. The peak computed vertical compressive strains, at the end of the web, computed with TW2-9, TW2-17, and TW2-17b were 5.2%, 10.4%, and 17.7%, respectively.

The effect of not considering mesh size effects was also investigated for the beam model of specimen TW2 of Case Study 1. Figure 10(b) compares the response of the beam models using two and four integration points, termed TW2-B2ip and TW2-B4ip, respectively. The stress-strain relationships of these two models were adjusted for size effects. A second model with four integration points was considered (termed TW2-B4ip-2) using the same stress-strain relationships used in the model with two integration points. As expected, the model TW2-B4ip-2 computed significant strength degradation at 2.3

times smaller drift ratio than the other two models. When the size effects are considered, the TW2-B2ip and TW2-B4ip models resulted in similar responses.

Figure 15(e) compares the computed monotonic response of the specimen of Case Study 3 using the F1-11-50 and F1-11-50NS models. Here, the F1-11-50NS model had a mesh identical to that of F1-11-50, but uses stress-strain relationships for concrete without accounting for size effects in the concrete. Thus it used the stress-strain relationships corresponding to an element with length of L_R = 600mm. As expected, the F1-11-50NS model computed initiation of strength degradation much earlier than F1-11-50 at drift ratio equal to 1.2%, as well as much more brittle behavior. Model F1-11-50NS computed 41% loss of strength at 1.5% drift, which is not observed in the F1-11-50 model.

Effect of the Angle of the Diagonal Truss Elements

For Case Study 3, models F1-11-45 and F1-11-50 had diagonal truss angles of about 45° and 50°, respectively. Figure 15(a) and (b) compares the computed response using these two models. The response of F1-11-50 model computed 3.4% smaller peak strength than the F1-11-45 model. The F1-11-50 model computed the first instance of web crushing during the first cycle at peak drift ratio of 2.2% at $\Theta = 1.28\%$, while the F1-11-45 model computed diagonal crushing during the first cycle at peak drift ratio of 2.2% at $\Theta = 2.0\%$ which is in better agreement with the instance of web crushing in the experimental response. The F1-11-50 model computed 38% strength degradation after computation of the first crushing of the diagonal trusses, which is in better agreement with the experimentally measured response than the 8% computed by the F1-11-45 model. Similar observations that increase of the angle of the diagonals resulted in softening of the diagonals at smaller displacement level as well as more strength degradation was made in the 2D model of Panagiotou et al. (2012).

Effect of Tension Strength of the Diagonal Truss Elements

In all case studies presented so far, zero tensile strength was used in the concrete material models of the diagonal truss elements. Figure 19 compares the monotonic computed response for the TW2-9 and F1-11-45 models of Case Studies 1 and 3, respectively, with and without tension strength in the diagonal elements. After tensile cracking, the concrete stress reduces linearly with increase of strain and becomes zero at strain $2\varepsilon_{cr}(600/L)$, where ε_{cr} the cracking strain of the concrete in tension and L is the diagonal element of length in mm. Both cases demonstrate that considering the tensile strength in the diagonal elements increased the initial stiffness by less than 40% for small lateral deformations corresponding to drift ratios less than 0.25%. For drift ratios larger than 0.5%, the effect was negligible.

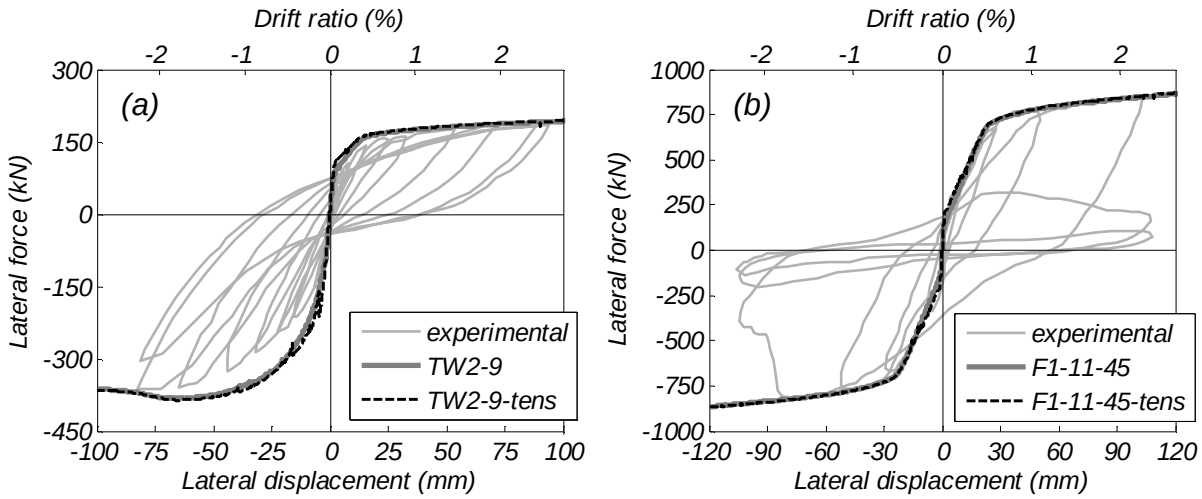

Figure 19. Effect of considering the tensile strength of the concrete diagonals in monotonic response: (a) Case Study 1 – TW2-9; and (b) Case Study 3 – F1-11-45.

Effect of Number of Integration Points

Figure 20 compares the monotonic computed force-displacement response of models TW2-9, TW2-17, and F1-11-45models using two or four integration points in the beam elements. The stress-strain relationship of concrete in each beam element was adjusted to account for the mesh size effect (as described in the *Mesh Size Effect* section). BTMs TW2-9-4ip, TW2-17-4ip, and F1-11-45-4ip with four integration points resulted in 5.6%, 8.1, and 7.2% larger peak strength, respectively, than the corresponding models with two integration points.

Since a fine mesh was used in all models in this study, two integration points are suggested, resulting in faster computation and less problems in terms of numerical convergence. The error in accuracy by using two integration points is not an issue for the level of mesh refinement used. As also presented in Neuenhofer and Filippou (1997) when the number of integration points decreases the increase of error in accuracy of computation decreases significantly with increase of number of elements used to represent a component of specific length. Large number of integration points in the short-length beam elements may result in localization issues.

Figure 17(c) compares the computed strain histories of Case Study 3 using the F1-11-45 model and the F1-11-45-4ip model that used four integration points in the beam elements. The strains shown were taken from the integration point closest to the base for longitudinal strains, and the integration point closest to the center of the web for transverse strains. As expected, the maximum computed strains at the location of gauges *sg1*, *sg2*, and average of *sg3* and *sg4* at the first cycle of 2.2% drift ratio using the F1-11-45-4ip model were 19.6%, 15.7%, and 49.1% larger than these of the F1-11-45 model because of the smaller effective lengths used in the former.

The effect of number of integration points for the fiber-section beam models was also investigated for specimen TW2, see Figure 10(b). The effect of number of integration points was not as important as was found in the beam-truss model. The four integration point model resulted in 2.3% larger peak strength and slightly larger deformations at initiation of the sudden strength degradation. Shown in Figure 18(b), the number of integration points had a negligible effect in the computed response for the beam model of Case Study 3.

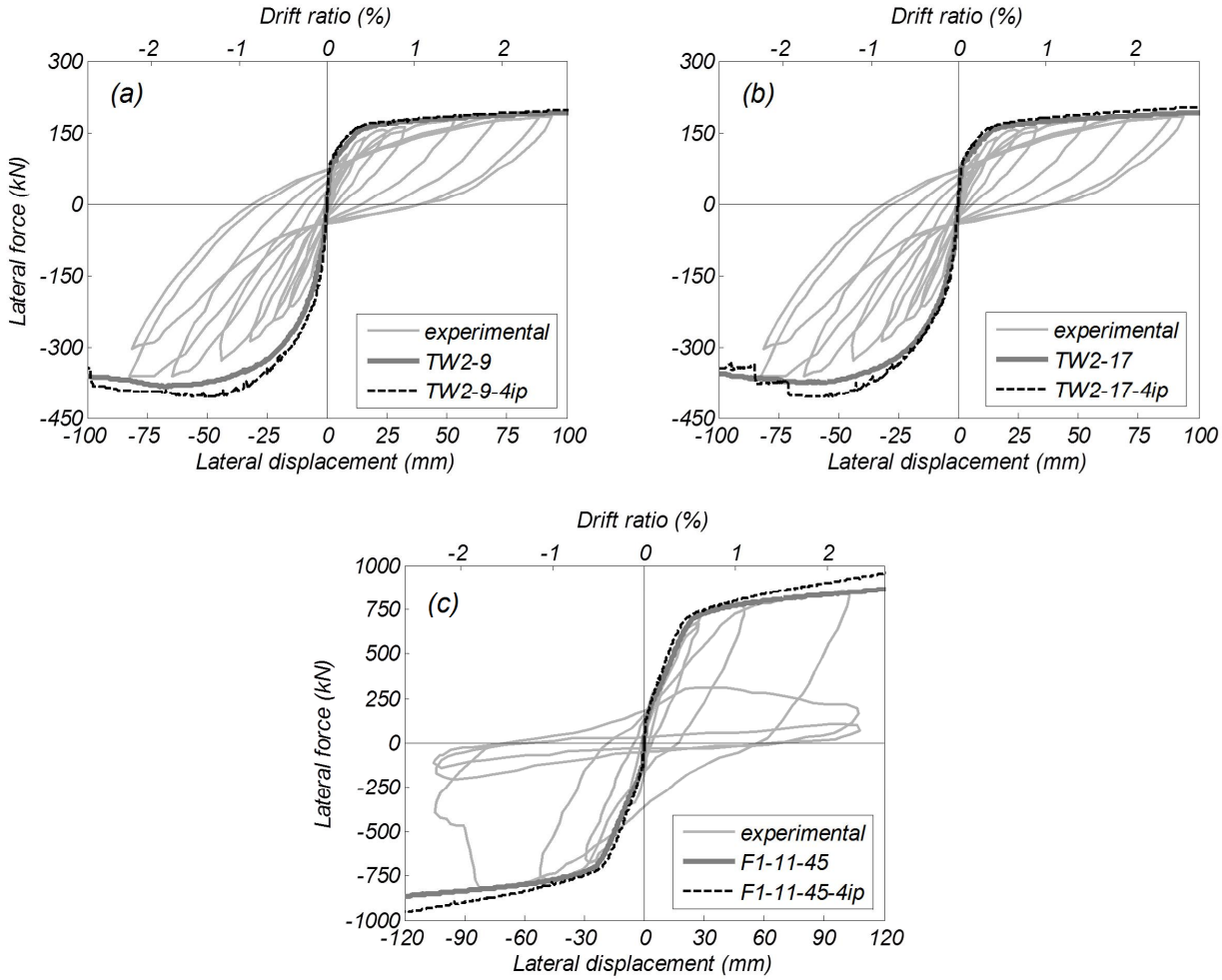

Figure 20. Effect of number of integration points in beam elements of the beam-truss models for monotonic response: (a) Case Study 1 – TW2-9; (b) TW2-17; and (c) Case Study 3 – F1-11-45.

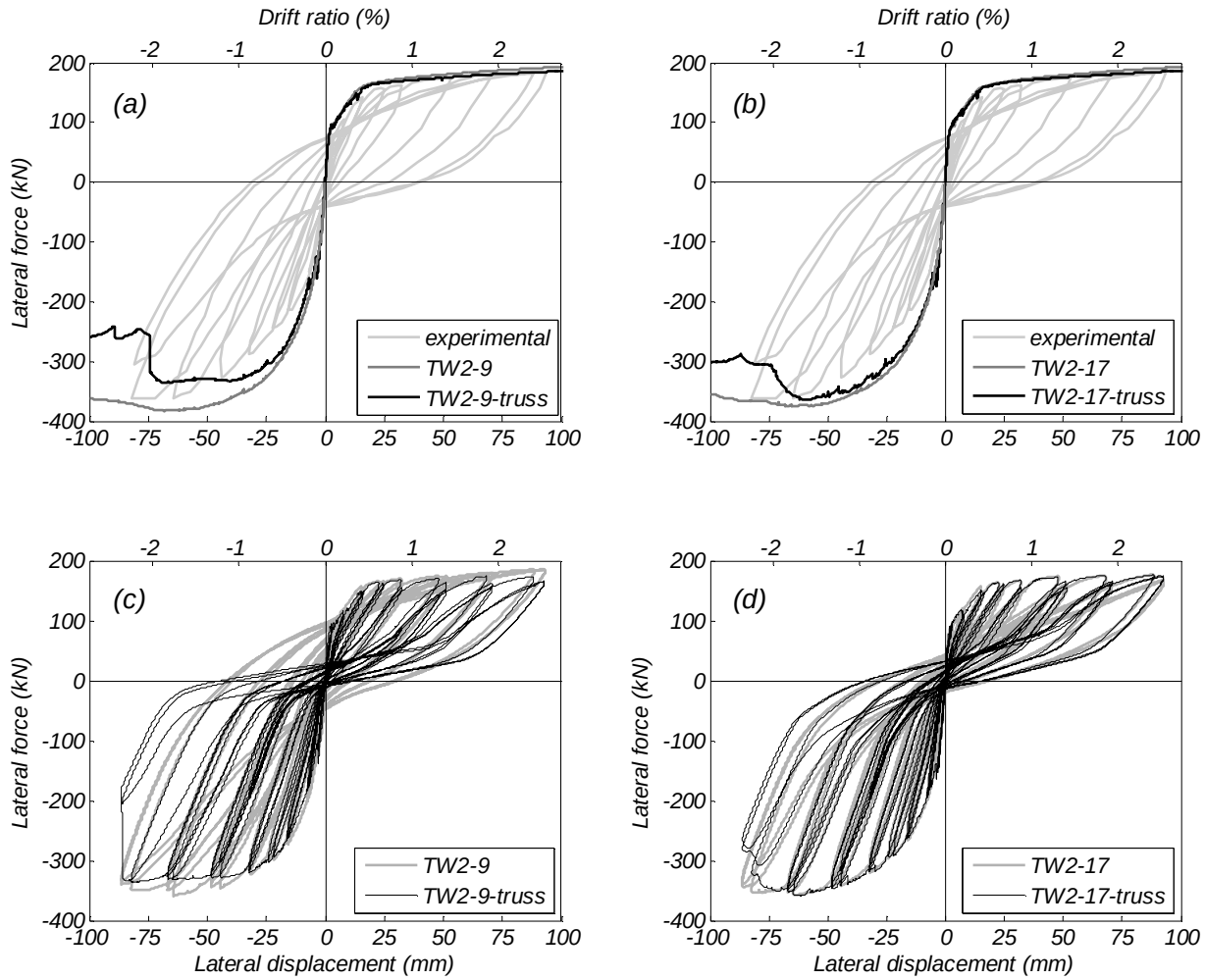

Figure 21. Effect of using truss elements, instead of vertical and horizontal beams, only in the web, for specimen TW2 of Case Study 1: (a) TW2-9 monotonic response; (b) TW2-17 monotonic response; (c) TW2-9 cyclic response; and (d) TW2-17 cyclic response.

Effect of Flexural Rigidity of Beams

The effect of using truss elements instead of beams for some of the vertical and horizontal elements was investigated for BTMs TW2-9 and TW2-17 of Case Study 1. A variation of the beam-truss models for TW2-9 and TW2-17 was considered, termed TW2-9-truss and TW2-17-truss, respectively, using truss elements for the vertical and horizontal elements in the web. Both models retained the horizontal and vertical beams in the flange to capture the out-of-plane contribution of the flange.

Figure 21 shows the computed monotonic and cyclic response for TW2-9-truss and TW2-17-truss compared to the experimental results and to the response of the original BTMs. Comparing Figure 21(a) and (b), it can be seen that using truss elements instead of beam elements in the web had a greater effect on the model with coarser mesh, which was expected. Using vertical truss elements in the TW2-9-truss

model resulted in 3.6% and 12.1% smaller peak lateral strength compared to TW2-9 model for the positive and negative direction of the monotonic response, respectively. For the cyclic response, the corresponding reduction in lateral strength was 6.4%, and 7.6%, respectively. The TW2-17-truss model resulted in 3.3% and 2.5% smaller peak lateral strength compared to the TW2-17 model for the positive and negative direction of monotonic response, respectively. The effect of using vertical truss elements in TW2-17 was negligible for the cyclic response.

Conclusions

This report described a three-dimensional (3D) beam-truss model (BTM) for non-planar RC walls. The model used nonlinear fiber section Euler-Bernoulli beam-column elements in the vertical and horizontal directions to represent concrete and reinforcing steel in the corresponding directions, and nonlinear truss elements to represent the diagonal field of concrete in compression. The model accounted well for the effects of flexure-shear interaction by computing the stresses and strains of steel and concrete in the vertical, horizontal, and diagonal directions, and by accounting for the effect of normal tensile strain on the compressive behavior of the concrete diagonals. The model also accounted for mesh size effects by having the softening branches of the concrete stress-strain material models dependent on the length of the elements. The efficacy of the model was investigated comparing the computed response using the BTM with the experimentally measured response of three non-planar RC walls subjected to cyclic loading having a T- U-, and I-shape section, respectively. The experimentally observed failure mode of the latter two walls was due to diagonal web crushing, while the contribution of the flange was important for the response of the first wall. The response of the three walls using existing nonlinear fiber-section Euler-Bernoulli beam models was also computed. The following conclusions were drawn:

1. The BTM computed very satisfactorily the cyclic force-displacement response of the three specimens. The difference between the computed and experimentally measured peak lateral strength was less than 1%, 3%, and 5% for the specimens of Case Studies 1, 2, and 3, respectively. The model in very good agreement with the experimental response, computed crushing of the diagonal concrete of the U- and I-shape section walls of Case Studies 2 and 3, respectively, for cycles with peak drift ratios equal to 3% and 2.2%, respectively.

2. The TW2-17 and F1-19-45 models computed strain histories that were in satisfactory agreement with the experimentally measured response. For the T-shape section wall, the computed and measured strains along the flange were compared and the TW2-17 model computed strains less than 24% different than the measured response for drift ratios up to 2.0%. At 2.5% drift ratio, the computed strain in the middle of the flange was 43% smaller than the experimentally measured response. For the I-shape section

wall, the F1-19-45 model computed strains in the vertical and horizontal directions, which differed less than 56%, and 42%, respectively, than the experimentally measured response at the first cycle with peak drift ratio 2.2%. A specific level of mesh refinement was required to achieve this level of accuracy in the computation of strains. The ratios of element lengths to the length of the wall, r_L, ranged between 9.9% and 16.5% for TW2-17 and between 9.0% and 13.7% for F1-19-45. The ratios of element lengths to the height of the wall, r_H, ranged between 3.3% and 5.5% for TW2-17 and between 3.8% and 5.9% for F1-19-45. The lower level agreement between measured and computed strains, than the level of agreement observed for the force-displacement response, it was partially due to the effect of bond slip which was not considered in the model.

3. For the T-shape section wall, the beam-truss models resulted in strength overestimation for drift ratios up to 1.5% for the direction of the response with flange in tension. The overestimation was equal to 13% and 6% at drift ratios 1.0% and 1.5%, respectively. This is mainly due to the overlap of areas of concrete in the vertical, horizontal, and diagonal elements of this model. Overestimation of strength and stiffness was also observed in the other two cases studies, but it was negligible (less than 5%) for drift ratios larger than 0.5%.

4. Mesh size effects were important for the computation of the force-displacement and strain responses when softening of materials was a factor. For the T-shape section wall of Case Study 1, refining the mesh by two times without changing the stress-strain relation of concrete resulted in computation of diagonal web crushing at a displacement 21% smaller than computed by the coarse mesh and 2.2 times more abrupt strength degradation.

5. The effect of magnitude of the angle of the diagonals, considered only for Case Study 3, affected the displacement level at which softening and crushing of the concrete diagonals occurred as well as on the level of brittleness of the force-displacement response. The angles of the diagonals of the models considered in the three Case Studies ranged between 41^o and 50^o.

6. Use of fiber-section Euler Bernoulli beam models resulted in 6.7%, 22%, and 20% larger lateral strength than the experimentally measured response for Case Studies 1, 2, and 3, respectively. Due to the inherent limitation to compute strains and consider equilibrium in the horizontal and diagonal directions, this model could not compute the failure mode of diagonal concrete crushing that occurred in the U- and I-shape sections walls of Case Studies 2 and 3. For the T-shape section wall, this model resulted in 35% overestimation of strength at 1.0% drift ratio for the direction of the response with the flange in tension and computed initiation of lateral strength degradation at a 50% smaller drift ratio than what is experimentally observed. Significant differences were observed between experimentally measured and computed cyclic responses at all displacement levels, especially for the T- and I-shape section walls.

References

1. American Concrete Institute (ACI). (2011). "Building code requirements for structural concrete," *ACI 318-11*, Farmington Hills, Mich., 503 pp.

2. Balkaya, C., and Kalkan, E. (2004). "Three-dimensional effects on openings of laterally loaded pierced shear walls." *Journal of Structural Engineering*, 130(10), 1506-1514.

3. Barbosa, A. R. (2011). "Simplified vector-valued probabilistic seismic hazard analysis and probabilistic seismic demand analysis: application to the 13-story NEHRP reinforced concrete frame-wall building design example." Ph.D. Thesis, Department of Structural Engineering, University of California, San Diego.

4. Barzegar, F., and Maddipudi, S. (1997). "Three-dimensional modeling of concrete structures. II: Reinforced concrete." *Journal of Structural Engineering*, 123 (10), 1347–1356.

5. Bazant, Z.P. and Ceolin L. (1979). "Blunt crack propagation in finite element analysis." *Journal of the Engineering Mechanics Division, ASCE*, 105(2), 297-315.

6. Bazant, Z. P. and Planas, J. (1998). "Fracture and size effect in concrete and other quasibrittle materials." Boca Raton, FL: CRC Press.

7. Beyer, K., Dazio, A., and Priestley, M. J. N. (2008a). "Quasi-static cyclic tests of two U-shaped Reinforced Concrete Walls." *Journal of Earthquake Engineering*, 12(7), 1023-1053.

8. Beyer, K., Dazio, A., and Priestley, M. J. N. (2008b). "Inelastic Wide-Column Models for U-Shaped Reinforced Concrete Walls." *Journal of Earthquake Engineering*, 12(S1), 1-33.

9. Cervenka, V., and Gerstle, K. H. (1971). "Inelastic analysis of reinforced concrete panels: theory." *IABSE Publications*, 31-II, 31-45.

10. Cervenka, V., and Gerstle, K. H. (1972). "Inelastic analysis of reinforced concrete panels: experimental verification and application." *IABSE Publications*, 32, 25-39.

11. Clough, R. W., King, I. P., and Wilson, E. L. (1964). "Structural analysis of multistory buildings." *Journal of the Structural Division, ASCE*, 90(ST3), 19-34.

12. Coleman, J. and Spacone, E. (2001). "Localization issues in force-based frame elements." *Journal of Structural Engineering*, 127(11), 1422-1425.

13. El-Tawil, S., Kuenzli, C. M., and Hassan, M. (2002). "Pushover of hybrid coupled walls. I: design and modeling." *Journal of Structural Engineering*, 128(10), 1272-1281.

14. Eligehausen, R., Genesio, G., Ožbolt, J., and Pampanin, S. (2009). "3D analysis of seismic response of RC beam-column exterior joints before and after retrofit." In Alexander et al (eds) *Concrete Repair, Rehabilitation and Retrofitting II. London: Taylor & Francis Group.*

15. Filippou, F. C., Popov, E. P., and Bertero, V. V. (1983). "Effects of bond deterioration on hysteretic behavior of reinforced concrete joints". Report EERC 83-19, Earthquake Engineering Research Center, University of California, Berkeley.

16. Giberson, M. F. (1969). "Two Nonlinear Beams with Definitions of Ductility." *Journal of the Structural Division, ASCE*, 95(2), 137-157.

17. Hassan, M. and El-Tawil, S. (2003). "Tension flange effective width in reinforced concrete shear walls." *ACI Structural Journal*, 100(3), 349-356.

18. Hidalgo, P. A., Jordan, R. M., and Martinez, M. P. (2002). "An analytical model to predict the inelastic seismic behavior of shear-wall, reinforced concrete structures." *Engineering Structures*, 24 (1), 85-98.

19. Hoshikuma, J., Kawashima, K., Nagaya, K., and Taylor, A. W. (1997). "Stress-strain model for confined reinforced concrete in bridge piers." *Journal of Structural Engineering*, 123(5), 624-633.

20. Kang, Y. J. (1977). "Nonlinear geometric, material and time dependent analysis of reinforced and prestressed concrete frames." UC-SESM Report No. 77-1, University of California, Berkeley.

21. Koutromanos, I. and Shing, P. B. (2012). "A cohesive crack model to simulate cyclic response of concrete and masonry structures." *ACI Structural and Materials Journal*. Accepted for publication.

22. Kwak, H. G. and Kim D. Y. (2004). "Material nonlinear analysis of RC shear walls subject to cyclic loadings." *Engineering Structures*, 26(11), 1426-1436.

23. Lykidis, G. C., and Spiliopoulos, K. V. (2008). "3D solid finite-element analysis of cyclically loaded RC structures allowing embedded reinforcement slippage." *Journal of Structural Engineering*, 134(4), 629-638.

24. MacLeod, I. A. (1973) "Analysis of shear wall buildings by the frame method." *Proceedings of the Institution of Civil Engineers*, 55(2), 593-603.

25. Maekawa, K., Pimanmas, A., and Okamura H. (2003). "Nonlinear mechanics of reinforced concrete." New York, NY: Spon Press. 721 pp.

26. Mander, J. B., Priestley, M. J. N., and Park, R. (1988). "Theoretical stress-strain model for confined concrete," *Journal of Structural Engineering*, 114(8), 1804-1826.

27. Martinelli, L. (2008). "Modeling shear–flexure interaction in reinforced concrete elements subject to cyclic lateral loading." *ACI Structural Journal*, 105(6), 675-684.

28. Mazars, J., Kotronis, P., Ragueneau, F., and Casaux G. (2006) "Using multifiber beams to account for shear and torsion. Applications to concrete structural elements." *Computer Methods in Applied Mechanics and Engineering*, 195(52), 7264-7281.

29. McKenna, F., Fenves, G. L., Scott, M. H., and Jeremic, B. (2000). "Open system for earthquake engineering simulation." <http://opensees.berkeley.edu>

30. Miki, T. and Niwa, J. (2004). “Nonlinear analysis of RC structural members using 3D lattice model,” *Journal of Advanced Concrete Technology*, 2 (3), 343-358.

31. Milford, R.V. and Schnobrich, W. C. (1985) “The application of the rotating crack model to the analysis of reinforced concrete shells.” *Computers & Structures*, 20 (1-3), 225-234.

32. Mosalam, K., Mahin, S. A., and Rojansky, M. (2003). “Evaluation of seismic performance and retrofit of lightweight reinforced concrete shearwalls.” *ACI Structural Journal*, 100 (6), 1-11.

33. Neuenhofer, A. and Filippou, F. C. (1997). “Evaluation of nonlinear frame finite-element models.” *Journal of Structural Engineering*, 123(7), 958–966.

34. Neuenhofer, A. and Filippou, F. C. (1998). “Geometrically nonlinear flexibility-based frame finite element.” *Journal of Structural Engineering*, 124(6), 704-711.

35. Oesterle, R. G., Fiorato, A. E., Johal, L. S., Carpenter, L. S., Russell, H. G., and Corley, W. G. (1976). “Earthquake-resistant structural walls - tests of isolated walls.” Report to the National Science Foundation, Construction Technology Laboratories, Portland Cement Association, Skokie, Illinois.

36. Orakcal, K., Wallace, J. W., and Conte, J. P. (2004). “Nonlinear modeling and analysis of slender reinforced concrete walls.” *ACI Structural Journal*, 101(5), 455-465.

37. Ozbolt, J., Li, Y.-J., and Kozar, I. (2001). “Microplane model for concrete with relaxed kinematic constraint.” *International Journal of Solids and Structures*, 38, 2683-2711

38. Pagnoni, T., Slater, J., Ameur-Moussa, R., and Buyukozturk, O. (1992). “A nonlinear three-dimensional analysis of reinforced concrete based on a bounding surface model.” *Journal of Computers and Structures*, 43(1), 1-12.

39. Palermo, D., and Vecchio, F. J. (2002b). “Behavior of three-dimensional reinforced concrete shear walls.” *ACI Structural Journal*, 99(1), 81-89.

40. Palermo, D. and Vecchio, F. J. (2007). “Simulation of cyclically loaded concrete structures based on the finite-element method.” *Journal of Structural Engineering*, 133(5), 728-738.

41. Panagiotou, M., Restrepo, J.I., Schoettler, M., and Kim G. (2012). "Nonlinear cyclic truss model for reinforced concrete walls." *ACI Structural Journal*, 109(2), 205-214.

42. Park, H., and Eom, T. (2007). “Truss model for nonlinear analysis of RC members subject to cyclic loading.” *Journal of Structural Engineering*, 133(10), 1351-1363.

43. Petrangeli, M., Pinto, P. E., and Ciampi, C. (1999a). “Fiber element for cyclic bending and shear of RC structures. I: Theory.” *Journal of Engineering Mechanics*, 125(9), 994-1001.

44. Petrangeli, M. (1999b). “Fibre element for cyclic bending and shear of RC structures. II: verification.” *Journal of Engineering Mechanics*, 125(9), 1002-1009.

45. Pietruszczak, S. and Mroz, Z. (1981). “Finite element analysis of deformation of strain softening materials,” *International Journal for Numerical Methods and in Engineering*, 17(3), 327-334.

46. Sittipunt, C. and Wood, S. L. (1995). “Influence of web reinforcement on the cyclic response of structural walls.” *ACI Structural Journal*, 92(6), 745-756.

47. Spacone, E., Ciampi, V., and Filippou, F. C. (1992). “A beam element for seismic damage analysis.” EERC Report 92/08 Earthquake Engineering Research Center, University of California, Berkeley.

48. Stevens, N. J., Uzumeri, S. M., Collins, M. P., and Will, T. G. (1991). “Constitutive model for reinforced concrete finite element analysis.” *ACI Structural Journal*, 88(1), 49-59.

49. Suidan M. and Schnobrich W. C. (1973). "Finite element analysis of reinforced concrete." *Journal of the Structural Division, ASCE*, 99 (10), 2109-2122.

50. Taylor, R. G. (1977). “The nonlinear seismic response of tall shear wall structures.” Ph.D. Thesis, Department of Civil Engineering, University of Canterbury, 207 pp.

51. Thomsen, J. H. and Wallace, J. W. (1995). “Displacement-based design for reinforced concrete structural walls: an experimental investigation of walls for rectangular and T-shaped cross-sections.” Report No. CU/CEE-95-06, Clarkson University.

52. Thomsen, J. H. and Wallace, J. W. (2004). “Displacement-based design of slender reinforced concrete structural walls - experimental verification.” *Journal of Structural Engineering*, 130(4), 618-630.

53. To, N. H. T., Ingham, J. M., Davidson, B. J., and Sritharan S. (2003). “Cyclic strut-and-tie modeling of reinforced concrete structures.” *Pacific Conference on Earthquake Engineering*, Paper No. 102, Christchurch, New Zealand, 2003, 9 pp.

54. Vallenas, J. M., Bertero, V. V., and Popov, E. P. (1979). “Hysteretic behavior of reinforced concrete structural walls.” Report No. UCB/EERC-79/20, Earthquake Engineering Research Center, University of California, Berkeley.

55. Vecchio, F. J., and Collins, M. P. (1986). “The modified compression field theory for reinforced concrete elements subjected to shear.” *Journal of the American Concrete Institute*, 83(2), 219-231.

56. Vidosa, F. G., Kotsovos, M. D., and Pavlovic, M. N. (1991). “Nonlinear finite-element analysis of concrete structures: performance of a fully three-dimensional brittle model.” *Computers & Structures*, 40(5), 1287-1306.

57. Zeris, C. and Mahin, S.A. (1988). “Analysis of reinforced concrete beam-columns under uniaxial excitation.” *Journal of Structural Engineering*, 114, 80.